Spring 1-1-2011

The Post-Fragmentation Probability Density for Bacterial Aggregates

Erin Byrne
University of Colorado at Boulder, erin.byrne@colorado.edu

THE POST-FRAGMENTATION PROBABILITY DENSITY FOR BACTERIAL AGGREGATES

by

ERIN BYRNE

B.S., Harvey Mudd College, 2000

M.S., University of Colorado, Boulder, 2005

A thesis submitted to the

Faculty of the Graduate School of the

University of Colorado in partial fulfillment

of the requirements for the degree of

Doctor of Philosophy

Department of Applied Mathematics

2011

This thesis entitled:
The Post-Fragmentation Probability Density for Bacterial Aggregates
written by Erin Byrne
has been approved for the Department of Applied Mathematics

David Bortz

John Crimaldi

Keith Julien

Manuel Lladser

John Younger

Date

The final copy of this thesis has been examined by the signatories, and we find that both the content and the form meet acceptable presentation standards of scholarly work in the above mentioned discipline.

Byrne, Erin (Ph.D., Applied Mathematics)

The Post-Fragmentation Probability Density for Bacterial Aggregates

Thesis directed by Prof. David Bortz

The post-fragmentation probability density of daughter flocs is one of the least well-understood aspects of modeling flocculation. This dissertation addresses the problem of determining an appropriate post-fragmentation probability density for common aggregate and biofilm forming bacterial species, such as **Klebsiella pneumoniae** and **Staphiloccocus epidermidis**. We seek to characterize the post-fragmentation density Γ using a three-pronged approach. First, we use 3D positional data of **K. pneumoniae** bacterial flocs in suspension and the knowledge of hydrodynamic properties of a laminar flow field and propose a model to construct a probability density of floc volumes after a fragmentation event, and we provide computational results which predict that the primary fragmentation mechanism for large flocs is erosion. Second, we consider an abstract evolution model for the flocculation dynamics and establish existence and well-posedness of solutions to the inverse problem. Third, a numerical approximation scheme based on the model is presented for inferring the post-fragmentation density from laboratory data for bacterial population size distribution, and the stability and robustness of identifying Γ is examined.

DEDICATION

To my sister, without whom this document would not exist.

ACKNOWLEDGEMENTS

Without the unwavering support of a large group of people, the work contained in these pages would not have occurred. My advisor David Bortz was not only pivotal to my choice to resume a Ph.D., but has guided me faithfully to this final destination. My collaborator John Younger and his Younger Lab at University of Michigan have not only provided me with data, but also camaraderie and friendships. The research was funded by NIH grant on the Biomechanics of Bacteremia, without which I would not have been able to support myself on this journey.

My family and friends have borne the heaviest burden over these several years. Without my sister Brooke Wagner (not to mention her husband Jason, and three beautiful children Mackenzie, Brandt, and Colton), this document and the degree it represents would not exist. They have been my rock, my safe haven, my support group, and my grounding. My brother Trey Byrne and my parents Roger Byrne and Linda Hoaglind, have also supported me throughout, providing the love and belief in myself that can only come from the people who have known you your entire life. The list of friends that at some point (or many points) improved my life and well-being over the course of this degree is illustrious and, unfortunately, too lengthy to mention all its members. But you know who you are. Thank you. I love you all.

CONTENTS

CHAPTER

FIGURES

Figure

CHAPTER 1

INTRODUCTION

In modeling the flocculation dynamics of bacterial and other biological and cellular aggregates in flowing aqueous environments, three important phenomena arise: growth, aggregation, and fragmentation [19]. Though much attention has been given to the dynamics of floc aggregation since von Smoluchowski published his coagulation equations in 1916 [82], the research into floc breakup has been less successful, as the complex, random nature of shear force-induced fragmentation makes the mathematics of floc breakup significantly more challenging than that of aggregation [83].

We describe the floc population using the population density function $b(t, x)$ which gives the number density of aggregates of volume x; that is, with volume in the small window of volumes between x and $x + dx$ (note that x is a continuous variable) at time t. Such a model, fitting into the broad aggregation-fragmentation theory, is commonly obtained in the current context as a limiting case of individual-based models [76, 19]. This size-structured population model is a special case of the Sinko-Streifer model first introduced 1967 ([78]) by James W. Sinko and William Streifer to describe the dynamics of single-species populations that display variation among different ages and sizes.

A vital component of the fragmentation kernel for mathematically modeling flocculation dynamics is the probability density of floc sizes after a fragmentation event occurs (the post-fragmentation probability density, $\Gamma(x; y)$), which defines the probability density for producing a daughter floc of size x from a floc of size y. This dissertation uses three

approaches to characterize the post-fragmentation density function $\Gamma(x; y)$. The approach utilized in Chapter 2 is constructive, and uses 3D positional data from real flocs in an algorithm that subjects the flocs to hydrodynamic forces and builds $\Gamma(x; y)$ from the resulting fragmentations. Chapter 3 is highly theoretical, defining an inverse problem for inferring Γ from the population model and showing existence and well-posedness of its solutions. We also define an approximate inverse problem and show general "method stability" for its implementation. In Chapter 4 the approximate inverse problem is implemented using nonlinear constrained optimization, and the effects of noise in the data and mesh size on the fitted solution are examined. In addition, the sensitivity of the population size distribution on the post-fragmentation density is investigated. Finally, we conclude with a discussion of some of the implications of this work and possible future directions.

1.1 Background

Fragmentation phenomena arise in a variety of areas. Similar to the study of the evolution of size-structured algal populations, fragmentation is found in the hyperbolic equations describing the coagulation of phytoplankton, a fundamental mechanism for vertical flux of carbon in the ocean ([1, 2, 8]). We also see fragmentation play an important role in the dynamics of cancer metastases, since destructive fragmentation of non-metastatic cells is observed when they interact with human blood vessels ([102, 24, 46]). A non-biological example of fragmentation behavior can be found in mining, where the post-blast particle size is directly related to the efficiency of a mine and used to optimize production costs ([34, 70]). Other examples include social networks, voting blocs, and even the genetic history of species, which all fragment for different reasons.

The work presented here addresses the task of characterizing the post-fragmentation density $\Gamma(x, y)$ to gain a better understanding of the types of fragmentation processes present. Because of the challenging nature of the characterization of floc break-up, a fragmentation mechanism is typically simply assumed and incorporated into the model [1, 8, 19, 40, 53,

61, 68, 86]. Many different functional forms of the post-fragmentation probability density are used in the literature and while we detail popular forms below, we direct the interested reader to the extensive reviews in [40, 74, 95, 87]. The same forms commonly appear for use in modeling both animate (e.g. algae [1, 63], bacteria [19], yeast [86]) and inanimate (polymer [40, 87]) material.

The two most prominently-used forms for $\Gamma(x; y)$ are a binary fragmentation density and the log-normal density. Binary fragmentation assumes a floc will fragment into two similarly sized daughter flocs, and its use is seen in models that consider individual fragmentation events. The log-normal distribution was proven by Kolmogorov [57] to be the limiting density for repeated, exhaustive binary fragmentation, and several authors including Lu and Spielman [61] and Pandya and Spielman [68] adopted this result for repeated floc erosion. One assumption which yields the log-normal density is homogeneity and does not hold for our bacterial flocs. As shown in Chapter 2, the predictions from our computations suggest that neither do single fragmentation events result in similarly-sized daughter flocs, nor does exhaustive fragmentation yield a log-normal size density.

There have been several studies concerning the fragmentation of an individual floc. Computational work has been conducted (for examples, see Potanin [72, 73], Higashitani and Iimura [43]) simulating the breakup process due to shear forces, but only flocs of generic spherical particles held together by short-range Van der Waal forces are simulated. Imaging analysis of the fragmentation process can be found in work by Blaser [16] and shows examples of both binary fragmentation and erosion in shear flow, but the experiments were performed with ferric hydroxide flocs, which are also held together by Van der Waal forces, and do not address a post-fragmentation density. We address this issue of translating individual fragmentation events into an overall population-level post-fragmentation density with the methodology presented in Chapter 2.

Experiments can often provide us population-level data for the distribution of floc sizes at various times. Kobayashi [55] conducted similar experiments to Blaser in a converging

flow, examining overall population fragmentation, but considered only the average floc size since the experiment could not allow for the tracking of individual fragmentation events. Since this type of population data can be theoretically acquired, we return to the population model for $b(t, x)$. The problem now becomes the framing of an inverse problem for estimating the post-fragmentation conditional probability measure from system observations.

We propose an approximation scheme for this inverse problem for the inference of the probability measure. Parameter estimation is an exceedingly common modeling concern, with a rich theoretical base (for example [1, 5, 11, 13, 9, 94], which provide only a small sampling of the available literature). Most parameter estimation problems are concerned with identifying a discrete number of values, but our problem is to infer a probability measure. The approach taken here is similar to that for identifying a single probability measure in Banks and Bihari [11] and a countable number of probability measures in Banks and Bortz [12], and we extend this theory to conditional probability measures. The infinite-dimensional nature of the solution space demands that computational efforts be focused on an approximation scheme, thus our theory includes the appropriate analysis for the general stability of the approximation.

When inferring a probability measure or distribution, it is common to find that distribution parameterized in some way (e.g. a normal distribution parameterized by its mean and variance), where only the parameters are fitted (e.g. [94, 5]). In contrast, the work presented here uses a nonparametric distribution and infers the function values for a discretization of the distribution (see [25] for more information on nonparametric distributions). This approach allows more freedom in the inference of the distribution by not assuming **a priori** a particular functional form.

When any parameter inference is being conducted, it is natural to want to understand how changes in the parameters affect the model solution. One way to address this concern is to perform a **sensitivity analysis**. Developed in the context of modern control theory, the sensitivity equations are found in a variety of fields including aerospace, mechanical and

electrical engineering [3, 23], and are often used in optimization and inverse problem theory [77]. The solution to these equations contain information regarding the sensitivity of our original system to changes in a particular parameter. Again, in this investigation the focus is not on a single parameter but a nonparameterized function, and the sensitivity analysis is adapted accordingly.

CHAPTER 2

MODEL FOR FLOC BREAK-UP

2.1 Introduction

The first chapter of this dissertation considers a representative example of a bacterial species, **Klebsiella pneumoniae**, that commonly grows in an aggregate community. This work is taken largely from our recently published manuscript [20] in PRE.

K. pneumoniae is an aggregate and biofilm forming organism common to fresh water environments, and also frequently encountered as a human pathogen [71, 62]. In human disease it is an important cause of biofilm-based intravenous catheter infections and therefore a common cause of disseminated bloodstream infections. **Klebsiella** is a typical member of the family **Enterobacteriaceae**, to which belong a number of problematic species for mankind, including **E. coli** (food borne diarrheal and urinary tract illnesses), **Salmonella** and **Shigella** (water borne diarrheal illness), **Yersinia** (plague), and **Erwinia** (an important group of agricultural pathogens). Relevant to the current discussion, a recent study (by the Younger and Solomon labs) carried out high-resolution confocal microscopic imaging analysis of **K. pneumoniae** aggregates. It is from these results that the current analysis proceeds.

Recall that the two most prominently used functional forms for $\Gamma(x, y)$ are binary and log-normal densities. For a single fragmentation event, the binary density is most common and assumes such an event results in two similarly-sized daughter flocs, i.e., the mean field approximation to a beta fragmentation process. When considering an unlimited cascade of fragmentation events, the log-normal is derived from assuming that cascade will result

in many small and few large daughter flocs. Kolmogorov [57] showed the log-normal density to be the limiting density for repeated, exhaustive binary fragmentation, and Lu and Spielman [61] and Pandya and Spielman [68] adopted this result for repeated floc erosion. One assumption which yields a log-normal density is homogeneity and does not hold for our bacterial flocs. The predictions from our computations suggest that neither do single fragmentations events result in similarly-sized daughter flocs nor does exhaustive fragmentation yield a log-normal size density.

The focus of this chapter is to construct a post-fragmentation particle size probability density for bacterial aggregates based on high resolution structural measurements of **K. pneumoniae**. We focus on particles in linear, laminar flow primarily for analytic simplicity, but note the potential relevance of this particular flow regime to one of **Klebsiella**'s most troublesome features, the tendency to invade the bloodstream of critically ill patients.

Section 2.2 describes the method used to construct the post-fragmentation probability density from the 3D positional data. Section 2.3 reports the results of the simulated floc breakup and discusses the implications of the findings. Finally, Section 2.4 summarizes the conclusions of this chapter.

2.2 Model and Methods

Our goal is to develop an analytic strategy for identifying breakage locations, calculating the associated stress due the hydrodynamic forces at work, and then using that information to predict if a fragmentation event will occur. This process must consider both the geometry and material properties of the floc as well as the hydrodynamic environment. Aggregates are discretized into a countable number of bacteria that are assumed to be non-breakable. **K. pneumoniae** is a cylindroid, roughly twice as long as wide, and we will assume that this shape does not significantly impact our results. While we have data on the 3D locations and orientation of the bacteria that constitute a given floc, the density and extent of the **extracellular polysaccharides** (EPS), or **biofilm**, is not observable

with current technology. We assume an EPS layer of uniform thickness encapsulating each bacterium, and no additional strength or structure is attributed to any overlapping regions. Lastly, note that in our analysis we do not consider the possibility of an EPS fragment (without bacteria) separating from the mother floc.

2.2.1 Description of the data

The 3D structural data of 39 aggregates were collected and imaged in the Younger and Solomon labs [27]. In brief, bacterial aggregates were obtained by growing organisms in defined media under gentle hydrodynamic conditions. These structures were fluorescently stained and then imaged with confocal microscopy to produce 3D image volumes containing each bacterium in an aggregate. Image analysis software [65] identified the Cartesian coordinates of the center of mass of each cell. Note that we use all 39 aggregates in the estimation of $\Gamma(x; y)$.

2.2.2 Breakage location identification

Our analysis of possible fragmentation locations is based entirely on the relative positions of the bacteria that constitute a given floc. The discretized nature of the bacteria allows us to characterize the aggregate as an undirected graph where the centers of mass of the individual bacteria are the nodes, and the pairwise connections between the centers of mass are the edges. Each edge is given a weight corresponding to the distance between the two bacteria it connects. A **spanning tree** of a graph is any subset of edges with no closed loops where the edges connect all the nodes in the graph. The **minimum spanning tree** (MST) is the spanning tree that minimizes the sum of the weights of the constituent edges and is unique for graphs with distinct edge weights. Further information on the MST and its properties can be found in [22].

By finding the MST using distances as the edge weights, we identify the smallest total distance needed to connect all the bacteria in the floc. We assume the longest edge in the

MST is the most likely to fragment first because it indicates the largest distance between neighboring bacteria. Conceptually, if the uniform EPS layer were reduced in thickness until a separation occurred, the first separation would be located on the longest edge of the MST.

We use Kruskal's algorithm [59] for finding the MST, and consider each edge in the MST as a candidate for fragmentation. The fragmentation plane is taken to be the perpendicular bisector of the edge and separates the floc into two daughter flocs. A sample floc from our data set, its bacterial centers of mass and the corresponding MST are depicted in Figure 2.2.1(a), while an alternative view with a candidate fragmentation plane $P_\perp$ is depicted in Figure 2.2.1(b).

2.2.3 Simplification of the model

Flocs come in all shapes and sizes, and this spatial variation makes calculating the exact hydrodynamic forces at work on the effective surface of the floc challenging. We therefore use an approximation which facilitates calculation while still capturing the general shape of the floc.

Optical observations [16] find that simple shear flow leads to rotation of the floc, and its motion can be understood by the behavior of a solid ellipsoid. We approximate the aggregate by an ellipsoid tumbling in a linear flow field as is assumed in [15, 16, 47] and validated in [55, 56]. To find a hydrodynamically equivalent ellipsoid, we use Principle Components Analysis (PCA) on the spatial data for centers of mass of the bacteria in the floc. PCA yields an orthogonal linear transformation that maps data to a new coordinate system such that each principle component sequentially accounts for as much of the variability as possible. On spatial data, PCA simply performs a coordinate rotation that aligns the transformed axes with the directions of maximum variance. Further information on PCA can be found in [51].

The floc is rotated to align the longest semi-axis (with length a_1) with the x-axis, the next longest (with length a_2) with the y-axis, and the shortest (with length a_3) with the z-axis. For visualization purposes, we depict in Figure 2.2.2 the rotated centers of mass

and semiaxes for an equivalent ellipsoid. We chose the magnitude of the semiaxes as twice the standard deviation along the principal components, though note that the calculation of the hydrodynamic forces depends only upon the ratio of the semi-axis lengths and not the lengths themselves (see Section 2.2.4). The surface of the aligned ellipsoid is denoted D and described by $D: \ \frac{x^2}{a_1^2} + \frac{y^2}{a_2^2} + \frac{z^2}{a_3^2} = 1$, where $a_1 \geq a_2 \geq a_3$.

Our focus is primarily on medium to large flocs, but for completeness small flocs are also considered in our analysis. Our results take the size of the mother floc into consideration, and we note the impact of finite-size effects in small flocs. When any semi-axis length is found to be less that one micron, the value is replaced with one micron to allow for the presence of the EPS. When only two bacteria make up a floc, using PCA to find the equivalent ellipsoid fails due to the lack of any variance of the data in the second and third principle directions. In this case, we assume the length of the first semi-axis to be half the distance between the two bacteria plus an additional one micron buffer for the EPS, and the second and third semi-axes to be one micron.

2.2.4 Hydrodynamic forces

The forces on the surface of an ellipsoid in a linear flow field are well understood [60, 17] and our criteria for floc breakage is determined by comparing floc strength to hydrodynamic forces. While the energy-based approach advocated in [6, 7] is more general, we consider only a laminar flow environment and not one with turbulent mixing. Thus the energy dissipation rates and the potential energy associated with the rupture need not be formulated for our case.

We consider the floc immersed in a linear shear flow field, represented by a 3x3 matrix, $\mathbf{G}$, where the (1,2) element is γ and all other elements are zero. The parameter γ is the constant fluid shear rate along the y-axis.

The center of mass of the floc is assumed to be moving with the flow, so the only hydrodynamic forces acting on the ellipsoid are due to rotation (Jeffery [50] provides a

formulation for this force). We assume the fluid's pressure on the ellipsoid is negligible. The rotational force on the surface of the ellipsoid is given by:

$$\mathbf{f_R} = 4\mu \left(\mathbf{A} - \sum_{k=1}^{3} \chi_k A_{k,k} \mathbf{I} \right) \mathbf{n} \tag{2.2.1}$$

where μ is the viscosity of the fluid, $\mathbf{n}$ is the normal vector to the surface of the ellipsoid, χ_k are elliptic integrals involving the semi-axis lengths, and $\mathbf{A}$ is a matrix linearly dependent on $\mathbf{G}$ and the semi-axis lengths. The formulations for χ_k and $\mathbf{A}$ can be found in Appendix A, adapted from Blaser [17]. We note that f_R depends only on the ratios of the semi-axis lengths and not the semi-axis lengths themselves.

If we constrain the net hydrodynamic torque to be zero, we can use the **Jeffery equations** to find the angular velocity, ω, of the ellipsoid. We assume the semi-axis a_3 and the vorticity vector of the shear flow are constantly aligned, reducing the Jeffery equations to a single equation for the angular velocity around the z-axis:

$$\omega_3 = \Omega_{1,2} + \frac{a_1^2 - a_2^2}{a_1^2 + a_2^2} E_{1,2} \tag{2.2.2}$$

where $E_{i,k}$ and $\Omega_{i,k}$ are the (i,k)-th entries of the rate-of-strain tensor $\mathbf{E} = \frac{1}{2}(\mathbf{G} + \mathbf{G}^{\mathrm{T}})$ and the vorticity tensor $\mathbf{\Omega} = \frac{1}{2}(\mathbf{G} - \mathbf{G}^{\mathrm{T}})$.

The formulation for the force is given in the body-fixed frame and the velocity gradient given in the laboratory frame $\mathbf{G'}$ must be rotated using the transformation $\mathbf{G} = \mathbf{R}\,\mathbf{G'}\,\mathbf{R}^{\mathrm{T}}$. Since we assume only rotation about the z-axis, the rotation matrix is given by:

$$\mathbf{R} = \begin{bmatrix} \cos\phi & \sin\phi & 0 \\ -\sin\phi & \cos\phi & 0 \\ 0 & 0 & 1 \end{bmatrix} \tag{2.2.3}$$

where ϕ is the counter-clockwise angle of rotation measured from the positive x-axis. The motion of the ellipsoid is then related to the angular velocity by the equation $\phi' = \omega_3$.

The forces calculated through this method are vector quantities of stress (force per unit area) on the surface of the ellipsoid and are visualized in Figure 2.2.3. Note that this formulation accounts for all shear flow-induced forces on the surface of the ellipsoid.

2.2.5 Construction of a post-fragmentation probability density

This section describes the procedure we use to construct the post-fragmentation probability density, $\Gamma(x; y)$, from the data. After finding the MST for one floc (Section 2.2.2), we find a hydrodynamically equivalent ellipsoid (Section 2.2.3), and calculate the stress on the surface of the ellipsoid (Section 2.2.4).

The longest edge in the MST is the largest distance between neighboring clusters of bacteria, and thus the perpendicular bisector ($P_\perp$) of that edge is a candidate separation plane for the floc. This plane divides the ellipsoid into two pieces, and integration of the forces normal to $P_\perp$ over each piece of the ellipsoid yields the total tensile force:

$$\mathbf{F}_\perp = \left| \iint_{D>P_\perp} \mathbf{f}_\mathrm{R} \cdot \mathbf{n}_\perp \, dA \right| + \left| \iint_{D<P_\perp} \mathbf{f}_\mathbf{R} \cdot \mathbf{n}_\perp \, dA \right|, \tag{2.2.4}$$

where $\mathbf{n}_\perp$ is the unit normal to $P_\perp$. Because the ellipsoid is in a laminar shear field, it rotates and we calculate the force over one period of motion, using the maximum value in the calculation of the maximum tensile stress, $\sigma_{\max}$.

The **rupture stress**, σ_r, of the EPS is the stress required for the EPS to separate, or rupture. When σ_r is exceeded, we say a fragmentation event has occurred. If $\sigma_{\max}$ for the longest edge in the MST does not exceed σ_r, we recursively consider $\sigma_{\max}$ for the next longest edge in the MST as a candidate for separation until σ_r is exceeded. When a fragmentation event occurs, the edge under consideration is removed from the MST, creating two disconnected graphs which represent the two daughter flocs formed by the fragmentation.

Each daughter floc is then considered to be a new floc for potential fragmentation and analyzed as such. If σ_r is never exceeded along any edge in the MST, we say the floc does not fragment.

We repeat this process for each floc and construct a normalized histogram of the daughter floc sizes relative to the mother floc. This relative size is determined from the fraction of the number of bacteria in the mother floc that are in each daughter floc.

The algorithm is outlined by the following pseudocode to facilitate understanding. A more detailed version of the algorithm can be found in Appendix B.

```
1  INPUT Flocs = List of flocs

2  WHILE  i ≤ (No. of flocs in Flocs)
3          Find MST for Flocs(i)
4          Find equivalent ellipsoid for Flocs(i)
5          FOR k = 1 : (No. of edges in MST)
6                  Find P⊥ for k^th longest edge (separation plane)
7                  σ_max = max tensile stress for separation plane
8                  IF σ_max ≥ σ_r
9                      → Fragmentation Event
10                     Add daughters to Flocs
11                     GOTO 14
12                 END IF
13         END FOR
14         i = i + 1
15 END WHILE
```

To allow for future laboratory comparison, we apply the algorithm to selected combina-

tions of fluid shear rates and feasible biofilm rupture stresses. We allow the biofilm rupture stress (σ_r) to vary between 1 Pa and 150 Pa and the fluid shear rate (γ) to vary between 10 s^{-1} to 500 s^{-1}.

2.3 Results and Discussion

We investigated the post-fragmentation probability densities, $\Gamma(x; y)$, for various combinations of fluid shear rate and biofilm rupture stress. In all cases we explored, the resultant probability densities predominantly exhibit fragmentations resulting in one daughter floc significantly larger than the other. This suggests that the primary type of fracture occurring is the erosion of small clumps of bacteria off the mother floc, where we define **erosion** to be any fracture where one daughter floc is at least three fold the size of the other daughter floc. In the following sections we investigate the dependence of the post-fragmentation probability density on the size of the mother floc and different combinations of fluid shear rate and biofilm rupture stress. We also examine the density of particle sizes after **exhaustive fragmentation**, which we define to be the result of repeated fragmentation until the hydrodynamic forces are insufficient to fragment any remaining flocs. Finally, we support our results by comparing them with the results from artificially-generated flocs constructed to have similar statistical properties of flocs acquired in the laboratory.

2.3.1 Dependence on mother floc size

The density $\Gamma(x; y)$ depends heavily on the size of the mother floc since it is dramatically different when one or two bacteria fragment from a mother floc with 100 bacteria than a mother floc with 5 bacteria. According to our definition, erosion is only possible for flocs with four or more bacteria and flocs consisting of two or three bacteria are unable to have any fragmentation event result in erosion. An example of a post-fragmentation density function using mother flocs of all sizes ($\sigma_r = 10$ Pa, $\gamma = 100\ s^{-1}$) is shown in Figure 2.3.1(a). The same density is also shown having been separated into mother flocs with 15 or greater bacteria

(Figure 2.3.1(b)) and those with fewer than 15 bacteria (Figure 2.3.1(c)).

If we consider only mother flocs with 15 or more bacteria, over 90% of the fractures can be classified as erosion. Even for mother flocs as small as 5 bacteria, over 80% of the fractures are due to erosion. The resulting shape is distinctive, with the highest probability occurring on either end of the domain and the lowest occurring in the center (similar to Figure 2.3.1(b)). For smaller mother flocs, the density is more uniform, with spikes at the fractions where it is possible to produce daughter flocs. For example, there are spikes at $\frac{1}{3}$ and $\frac{2}{3}$, reflecting mother flocs with 3 bacteria fracturing into daughter flocs with 1 and 2 bacteria respectively.

The inclusion of mother floc size as a parameter in the density is common practice in the literature. For example, a uniform density function for producing a daughter floc of size x from a mother floc of size y can be represented by $\Gamma(x; y) = y^{-1}$ for $x \in [0, y]$ (see [40] for a summary of forms).

We examine the heavy dependence on the mother floc size more closely by considering it as a parameter in the post-fragmentation density function. While the number of mother flocs of a specific size varies in our data, there is enough resolution to see the general shape of the density evolve with the size of the mother floc (Figure 2.3.2(a)). For small mother flocs, we observe large spikes at fractions of the mother floc size. As the mother floc size increases, the largest of these spikes moves toward the edges of the domain, similarly to several of the experimental results in [103] for densely packed flocs. This migration is indicative of the trend for daughter flocs with a small number of bacteria to erode from the mother floc (Figure 2.3.2(b)-(d)).

2.3.2 Dependence on fluid shear rate and biofilm rupture stress

As mentioned, there are slight differences in the density functions for different combinations of fluid shear rate and biofilm rupture stress. Figure 2.3.3 depicts sample combinations of γ and σ_r. A combination of high rupture stress and low fluid shear rate (depicted in

Figure 2.3.3 upper right, $\sigma_r = 15$ Pa, $\gamma = 50$ s^{-1}) reduces the number of small mother flocs and thus the corresponding Γ more closely resembles the density for only larger mother flocs seen in Figure 2.3.1(b). Fewer fragmentations occur because the hydrodynamic forces acting on the floc are weaker. Conversely, a combination of low rupture stress and high fluid shear rate (depicted in Figure 2.3.3 lower left, $\sigma_r = 5$ Pa, $\gamma = 150$ s^{-1}) increases the number of fragmentations of small flocs, resulting in a density resembling Γ for only small mother flocs (Figure 2.3.1(c)).

When considering a constant rupture stress value and allowing the shear rate to increase, we see similar fragmentation behavior among all stresses. The shift from large mother floc to small mother floc densities occurs near $\gamma = 10\sigma_r$. We also notice a large increase in the number of fragmentation events that occur, depicted for various (σ_r,γ) combinations in Figure 2.3.4. For high rupture stresses, the number of fragmentations can increase by a factor of 1000 as the shear rate increases from 10 s^{-1} to 500 s^{-1}. For low rupture stresses, there is little difference since even small stresses will cause a fragmentation to occur and the number of fragmentations is limited primarily by the number of bacteria present. Whenever more than 1000 fragmentation events occur, the density function is well represented by the example shown in Figure 2.3.2(a), and typically the number of fragmentations exceeds 1000 when $\gamma > 10\sigma_r$.

2.3.3 Particle density after exhaustive fragmentation

Many different functional forms of the post-fragmentation probability density have been used in the literature. As mentioned earlier, the two most common are binary and log-normal. For exhaustive fragmentation, our results do not convincingly match the log-normal density. We denote the exhaustive density as Γ_{EX}, the size density of daughter flocs after repeated fragmentation. Our computations suggest that Γ_{EX} exhibits many small and few large flocs. Figure 2.3.5(a) depicts a sample comparison between Γ_{EX} and a discretized log-normal density fit to Γ_{EX} for $\sigma_r = 10$ Pa, $\gamma = 150$ s^{-1}. The Hellinger distance [98] between

Γ_{EX} and the fitted log-normal density ranges between 0.13 and 0.74. While the asymptotic tails of Γ_{EX} and the log-normal densities do match, the majority of the probability in Γ_{EX} is not captured by log-normal.

Note that to allow comparison between Γ_{EX} and the log-normal, we discretized the log-normal density over a partition of the domain chosen to match the Γ_{EX} bins. Naturally, this does introduce some error, but it is on the order of the bin widths. Furthermore the derivation of the log-normal density assumes homogeneity of structure. As can be seen in Figure 2.2.1, **K. pneumoniae** flocs are heterogeneous; the fractal dimensions for our flocs range between 1.8 and 2.4.

2.3.4 Comparison with similar DLA-generated aggregates

To explore the possible effects on our results of having a sample size of 39 flocs, we artificially generated flocs for analysis and comparison with the laboratory-acquired flocs. An extension of Witten and Sanders's **diffusion limited aggregation** (DLA) algorithm [101] was implemented to construct these additional flocs. The DLA algorithm was modified in two ways. First, the restriction that particles be placed on a simple cubic lattice was removed, allowing new particles to be placed freely in space. Second, we allow the distance between particles as they are placed to vary, with the specific distance for each new placement being drawn from the distribution of edge lengths in the MSTs of the original 39 flocs. We do not consider the spatial distribution of edge lengths, allowing long edges to appear throughout the floc as is observed in our laboratory flocs. For further details on DLA, we direct the interested reader to [101, 41]

From more than 10,000 DLA-generated aggregates, we chose 1159 for analysis by comparing the distribution of edge-lengths in their MST to that of our laboratory-acquired flocs. We found the Hellinger distance between the edge-length distributions of each DLA-generated floc and the laboratory flocs. The range of Hellinger distances was 0.16 to 0.36, and we selected the flocs where the distance was less than 0.21. The fractal dimension was

also checked to ensure it lay in the range of fractal dimensions present in the laboratory-acquired flocs. The selected DLA-generated aggregates were then used in our algorithm for generating a post-fragmentation density function.

The resulting density function depicted in Figure 2.3.6(a) is consistent with the density function based on our laboratory-acquired flocs. All DLA-generated flocs showed the predominant fragmentation mechanism to be erosion. The Hellinger distance between the post-fragmentation density function for the laboratory-acquired flocs and that for the DLA-generated flocs for each mother floc size is shown in Figure 2.3.6(b). The increase in this value as the mother floc size increases can be attributed to the small number of mother flocs of a specific size in our laboratory data. The DLA-generated flocs clearly have the same fragmentation behavior as the laboratory-acquired flocs and support our results.

The DLA-generated flocs were also used to construct the density of particle sizes after exhaustive fragmentation, and these results are consistent with that of the laboratory-acquired flocs (Figure 2.3.5(b)). For the example densities shown in Figure 2.3.5, the Hellinger distance between the data and the fitted log-normal curve are 0.29 for the laboratory data and 0.26 for the artificial data, while the Hellinger distance between the densities for the laboratory and artificial data is merely 0.01.

2.4 Concluding Remarks

A methodology is proposed to predict bacterial floc fragmentation in laminar flow. The method is applied to **K. pneumoniae** flocs to construct a post-fragmentation density. Numerical results suggest that the primary fragmentation mechanism for medium to large biological flocs is erosion and not the splitting of the original floc into two similarly-sized daughter flocs, as is commonly assumed in the literature. Also, rupture stress, shear rate, and floc shape all appear to have minimal impact on the post-fragmentation probability density.

The limiting density of floc sizes Γ_{EX} after exhaustive fragmentation is also investigated

and the results are found to be inconsistent with the log-normal density frequently employed in the literature [61] [68]. Our results are supported by applying our algorithm to artificially-generated flocs with statistical properties similar to the flocs acquired in the laboratory.

Much of the previous work on floc fragmentation is based on the breakup of flocs whose structure is due to short-range van der Waals attractions. Conversely, the structure of bacterial flocs is based on polymer networks secreted by the bacteria themselves, and the deformation and rupture of polymer networks is fundamentally different [85]. While treatment of the flocs as brittle is simplistic, the proposed methodology forms the foundation for more accurate modeling of fragmentation.

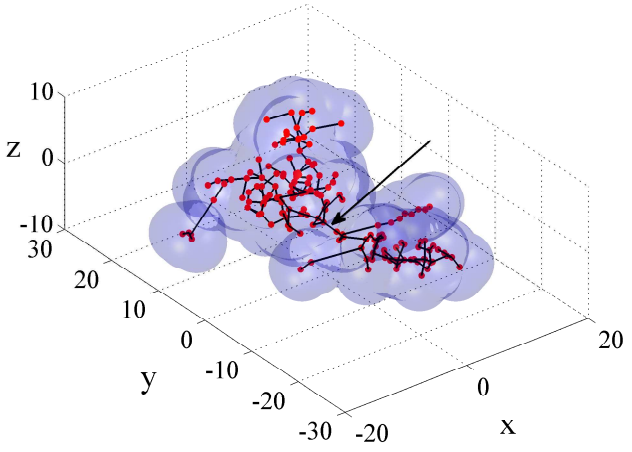

(a)

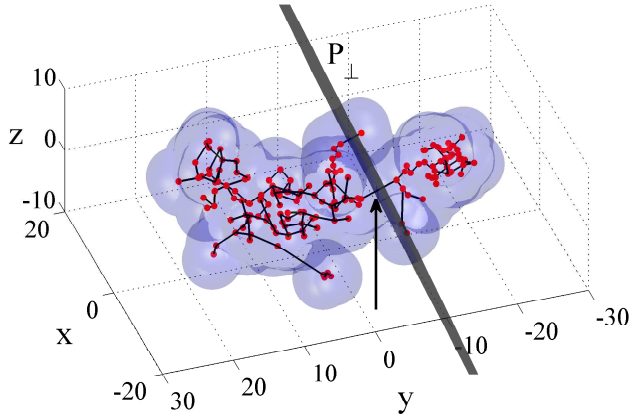

(b)

Figure 2.2.1: (a) Sample floc, enveloped by the effective surface of a uniform EPS layer (3D reconstruction). The red circles are the centers of mass of the bacteria in the floc and the blue lines are the edges that constitute the Minimum Spanning Tree (MST) of the centers of mass. (b) Alternate view of the same floc shown with a sample fragmentation plane $P_{\perp}$ determined by the edge in the MST identified by an arrow. Axes are in μm.

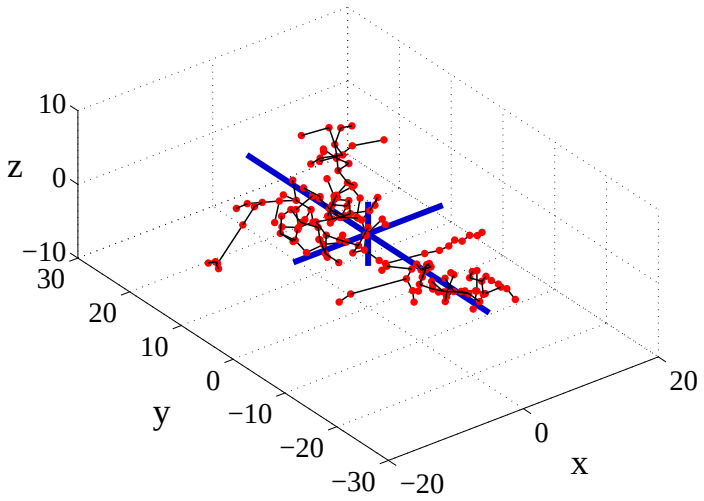

Figure 2.2.2: Sample floc depicting the centers of mass of the bacteria in the floc, the corresponding MST, and the semiaxes of a hydrodynamically equivalent ellipsoid as determined using Principle Components Analysis (PCA). Axes are in μm.

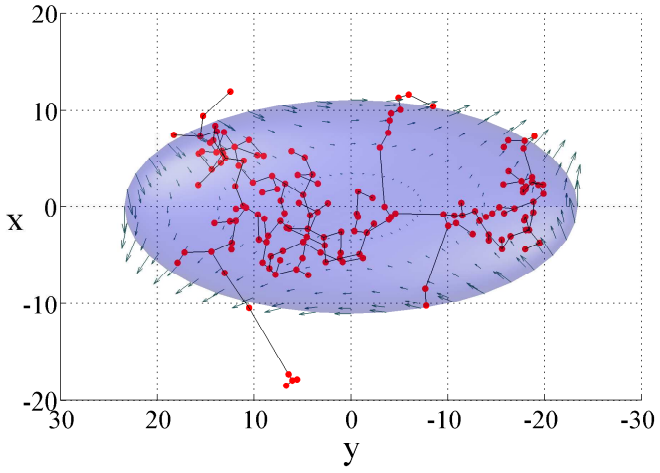

Figure 2.2.3: Sample floc depicting the centers of mass of the bacteria in the floc, the corresponding MST, a hydrodynamically equivalent ellipsoid, and sample ellipsoid surface force vectors (in Newtons) per unit area (longer vectors denote larger magnitude forces). Note that this figure is a projection of the data onto the xy-plane. The force vectors have no z component because of the ellipsoid's alignment with the flow and the largest forces occur around the ellipsoid's equator (the $a_1 \times a_2$ plane). Axes are in μm.

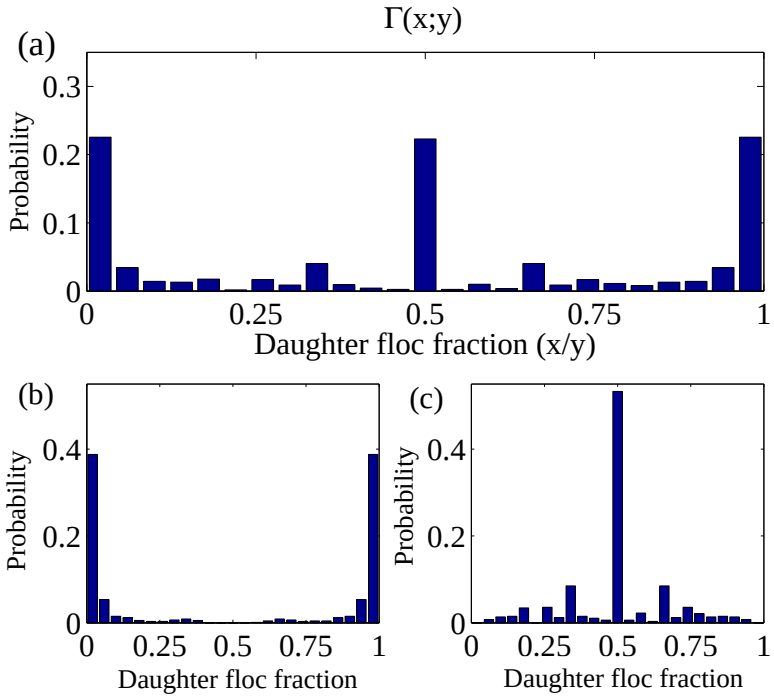

Figure 2.3.1: Sample post-fragmentation density function $\Gamma(x; y)$ ($\sigma_r = 10$ Pa, $\gamma = 100$ s^{-1}) considering (a) all mother flocs, (b) only mother flocs with 15 or more bacteria, and (c) only mother flocs with fewer than 15 bacteria. The x-axis is the size (number of bacteria) of a daughter floc as a fraction of the size (number of bacteria) of the mother floc.

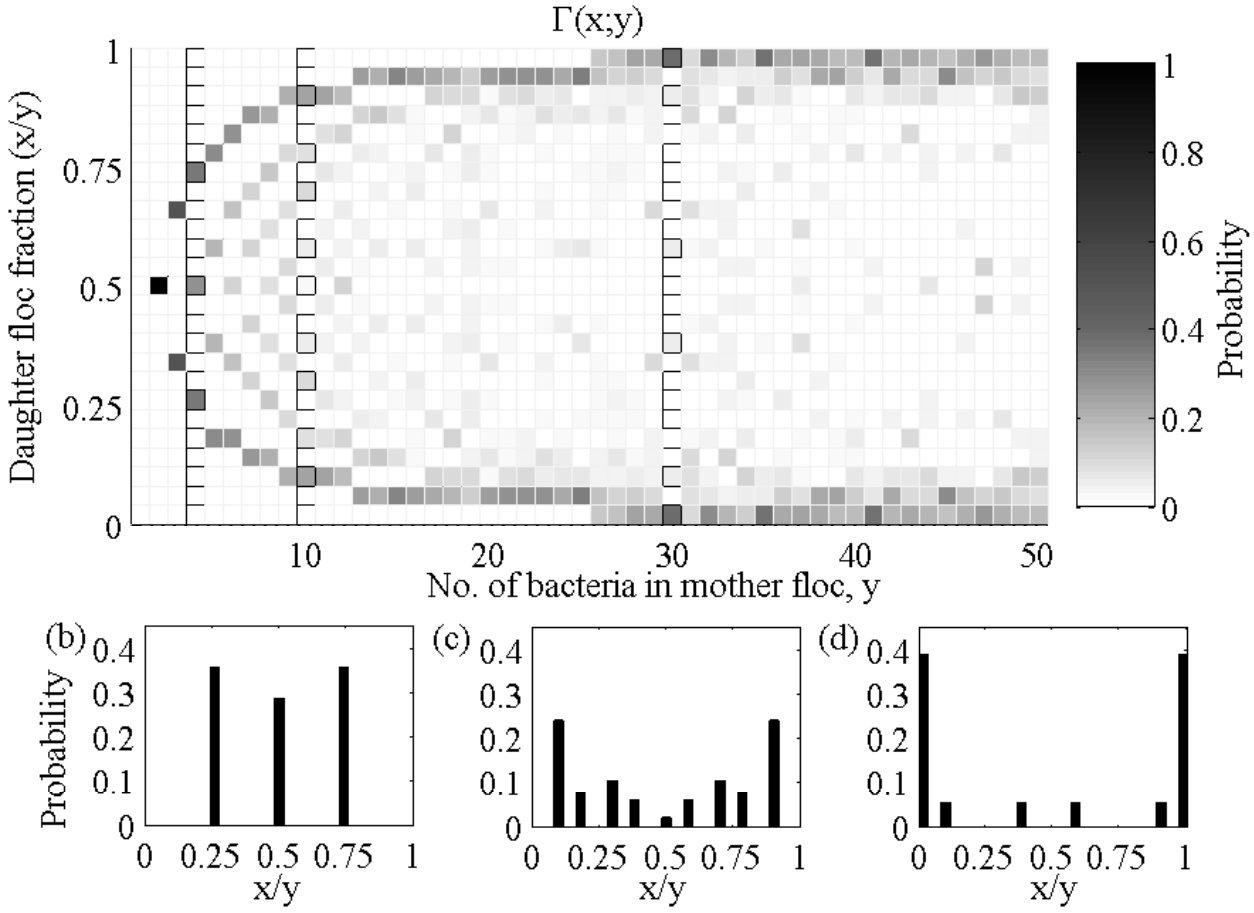

Figure 2.3.2: Sample post-fragmentation density function $\Gamma(x; y)$, depicting dependence on mother floc size, y. (a) Contour plot of the density. The x-axis is the mother floc size y and the y-axis is the size of a daughter floc as a fraction of the size of the mother floc, x/y. Also shown are (b) $\Gamma(x; 4)$, (c) $\Gamma(x; 10)$, and (d) $\Gamma(x; 30)$

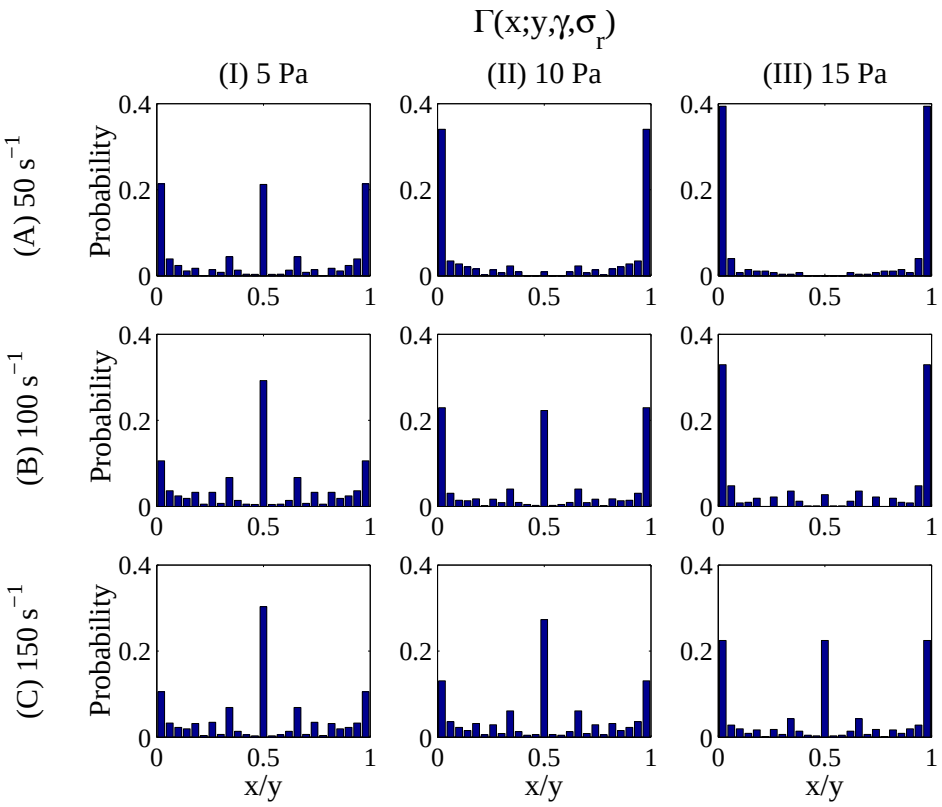

Figure 2.3.3: Post-fragmentation densities for various combinations of fluid shear rates (rows) and biofilm rupture stresses (columns). As fluid shear rate increases, the number of fragmentations increases (Figure 2.3.4) resulting in many small flocs fragmenting and a more centralized density function. Increasing rupture stress has the opposite effect, decreasing the number of fragmentations and resulting primarily in erosion.

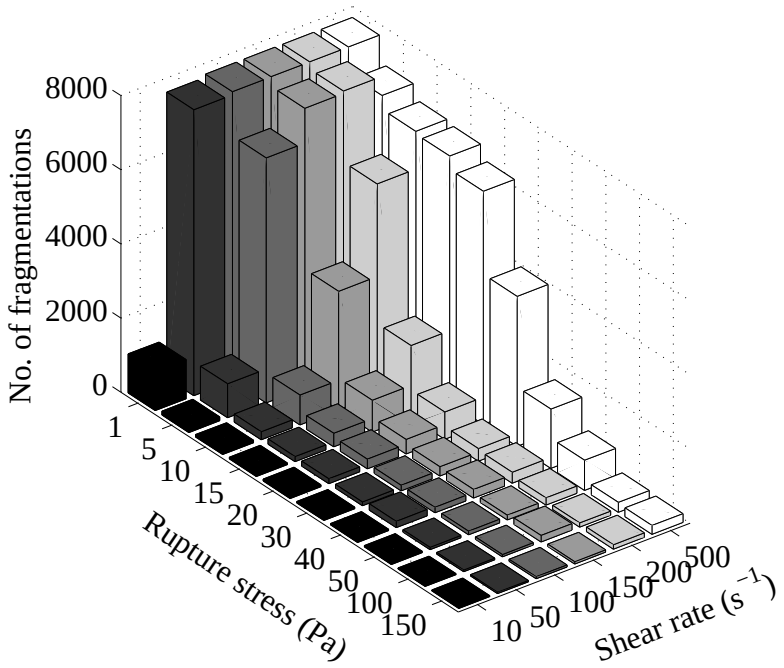

Figure 2.3.4: Total number of fragmentations that occur for different values of biofilm rupture stress (σ_r) and fluid shear rate (γ).

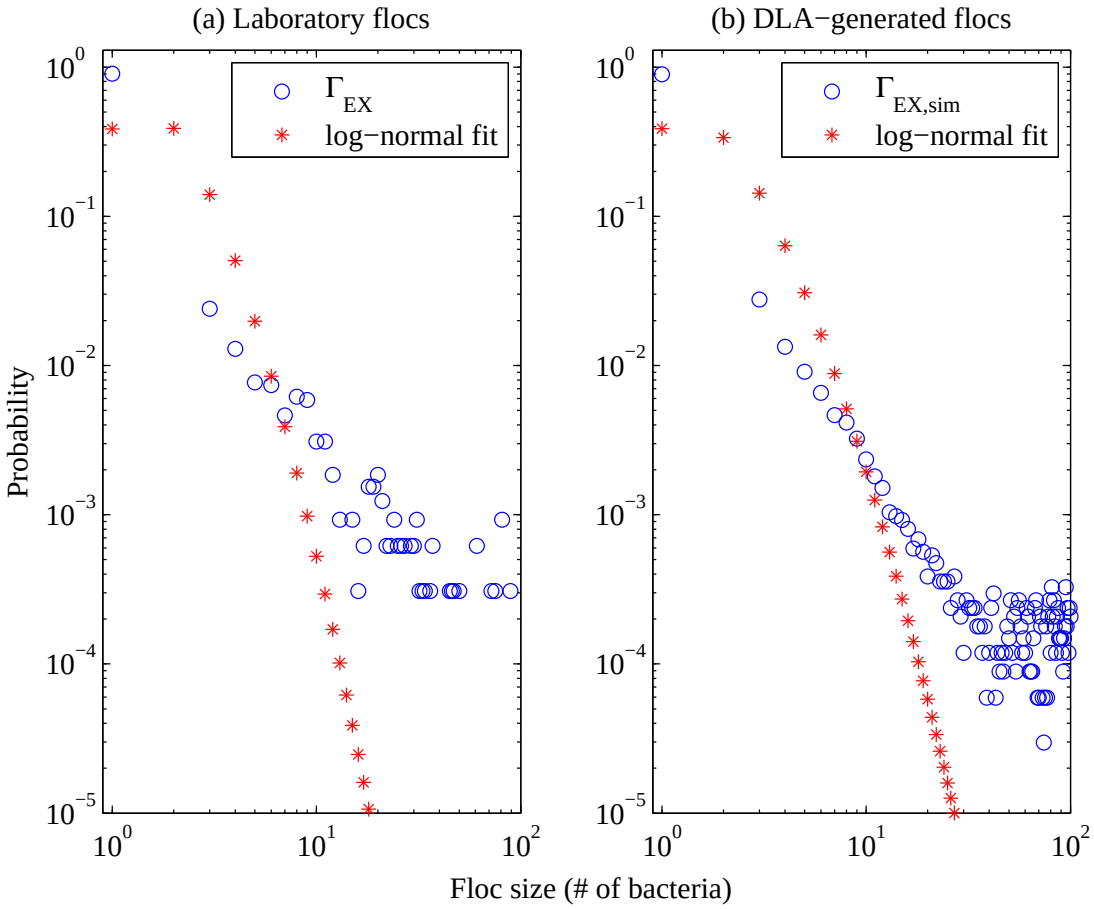

Figure 2.3.5: Sample floc size density ($\sigma_r = 10$ Pa, $\gamma = 150$ s^{-1}) after exhaustive fragmentation Γ_{EX} (blue circles), along with fitted, discretized log-normal densities (red stars). Densities are shown for (a) laboratory-acquired flocs and (b) DLA-generated flocs. The x-axis is the number of bacteria in a remaining floc and the y-axis is probability. Γ_{EX} reaches a lower bound near flocs of size 20 in the laboratory-acquired flocs and size 40 in the DLA-generated flocs due to the finite number of flocs present. Note the under-prediction of single bacteria flocs and flocs larger than 8, and the over-prediction of flocs between these values.

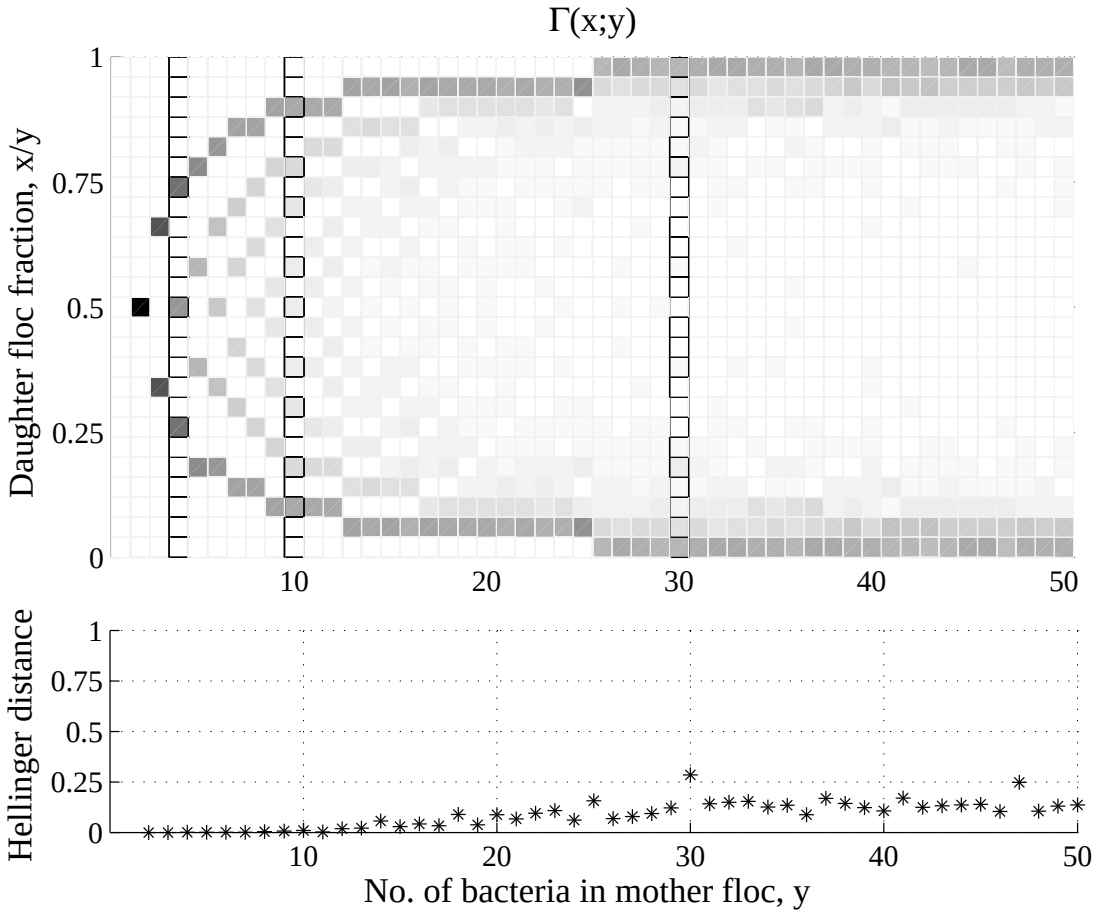

Figure 2.3.6: (a) Contour plot of the post-fragmentation density function constructed by our algorithm for 1024 DLA-generated flocs. The y-axis is the mother floc size and the x-axis is the size of a daughter floc as a fraction of the size of the mother floc. (b) The Hellinger distance between the post-fragmentation density functions of the laboratory-acquired flocs and the DLA-generated flocs as a function of mother floc size. The x-axis is mother floc size and the y-axis is the Hellinger distance.

CHAPTER 3

WELL-POSEDNESS AND EXISTENCE OF SOLUTIONS TO THE INVERSE PROBLEM

3.1 Introduction

The previous chapter outlined a methodology for constructing the post-fragmentation probability density from the geometry of the flocs and the physics of their environment. We now turn our attention to a mathematical model for the overall flocculation dynamics of bacterial aggregates. This model, presented fully in [19] and summarized in Section 3.2, considers all three processes important to flocculation: aggregation, fragmentation and growth. The post-fragmentation density $\Gamma(x, y)$ appears as one of two functions characterizing the fragmentation function, and our efforts focus on the inverse problem for the inference of $\Gamma(x, y)$ from the population size distribution $b(t, x)$ of bacterial aggregates over time.

In this chapter, we frame an inverse problem for estimating the conditional probability measures from system observations in measure-dependent nonlinear partial differential equations. We use the Prohorov metric, which is equivalent to weak convergence of measures, in a functional analytic setting and show well-posedness of the inverse problem. We also develop an approximation approach for computational implementation and show well-posedness of this approximate inverse problem, and the convergence of solutions to the approximate inverse problem to solutions of the original inverse problem. Our approach is similar to that for identifying a single probability measure in Banks and Bihari [11] and a countable number of probability measures in Banks and Bortz [12], and in this article we extend this theory to

conditional probability measures. Finally, we illustrate that the system described in (3.2.1)-(3.2.3) for the flocculation dynamics of bacterial aggregates in suspension is one realization of systems satisfying the hypotheses in our framework. The work presented in this chapter is taken largely from a recently submitted manuscript [18].

3.2 Background

This section summarizes the relevant mathematical model that serves as the foundation for the work presented in this chapter. Define $b(t,x)\,dx$ to be the number of flocculated bacterial biomasses having volume between x and $x+dx$ at time t. Then $b(t,x)$ is modeled by the system of equations (9) in [19], as shown below:

$$\begin{aligned} b_t &= -(G(x)b)_x + A(x,b) + F(x,b), && (3.2.1)\\ G(\underline{x})b(t,\underline{x}) &= 0, && (3.2.2)\\ b(0,x) &= b_0(x), && (3.2.3) \end{aligned}$$

where $b_0 \in L^1([\underline{x},\overline{x}],\mathbb{R}^+)$, $G(x)$ is the growth function, and $A(x,b)$ and $F(x,b)$ are the aggregation and fragmentation functions, respectively. The boundary condition $G(\underline{x})b(t,\underline{x}) = 0$ enforces the restriction that there is no biomass in the flask smaller than $\underline{x}$ that can grow bigger, i.e., there is a no-flux boundary condition at $\underline{x}$. The functions $A(x,b)$ and $F(x,b)$ are defined by:

$$\begin{aligned} A(x,b) &= A_{IN} - A_{OUT}, && (3.2.4)\\ A_{IN} &= \frac{1}{2}\int_{\underline{x}}^{x-\underline{x}} K_A(y,x-y)b(t,y)b(t,x-y)dy, \quad x \in [2\underline{x},\overline{x}], && (3.2.5)\\ A_{OUT} &= b(t,x)\int_{\underline{x}}^{\overline{x}-x} K_A(x,y)b(t,y)dy, \quad x \in [\underline{x},\overline{x}-\underline{x}], && (3.2.6) \end{aligned}$$

$$F(x,b) = F_{IN} - F_{OUT}, \tag{3.2.7}$$

$$F_{IN} = \int_{x}^{\overline{x}} b(t,y)K_F(y)\Gamma(x,y)dy, \quad x \in [\underline{x}, \overline{x} - \underline{x}], \tag{3.2.8}$$

$$F_{OUT} = \frac{1}{2}K_F(x)b(t,x), \quad x \in [2\underline{x}, \overline{x}], \tag{3.2.9}$$

where $\underline{x}$ and $\overline{x}$ are the minimum and maximum floc volumes, respectively. Also, K_A is the aggregation kernel, describing the rate at which flocs of volume x and y combine to form a floc of volume $x + y$, K_F is the fragmentation kernel, describing the rate at which a floc of volume x fragments, and $\Gamma(x,\ y)$ is the function describing the probability density of daughter flocs for the fragmentations of a parent floc of volume y. Note that for a given parent floc of volume y, Γ is simply a probability density in x on the interval $[\underline{x},\ y]$, and $\Gamma \equiv 0$ for $x \in (y,\ \overline{x}]$. As stated in the introduction, much of the framework for the inverse problem is based on the framework developed for the inverse problem for identifying a single probability measure in Banks and Bihari [11] and a countable number of probability measures in Banks and Bortz [12].

3.3 Well-Posedness of the Inverse Problem

We begin be considering the model in Equations (3.2.1)-(3.2.3). More specifically, we consider the inverse problem for inferring the post-fragmentation density function $\Gamma(x,y)$ from laboratory data. Considering the post-fragmentation cumulative distribution $F(x,y)$ is equivalent to considering $\Gamma(x,y)$ as they are related in the traditional way ($F(x,y) = \int_{\underline{x}}^{x} \Gamma(\xi,y)\,d\xi$). As stated in the introduction, much of the framework for the inverse problem is based on the framework developed for the inverse problem for identifying a single probability measure in Banks and Bihari [11] and a countable number of probability measures in Banks and Bortz [12].

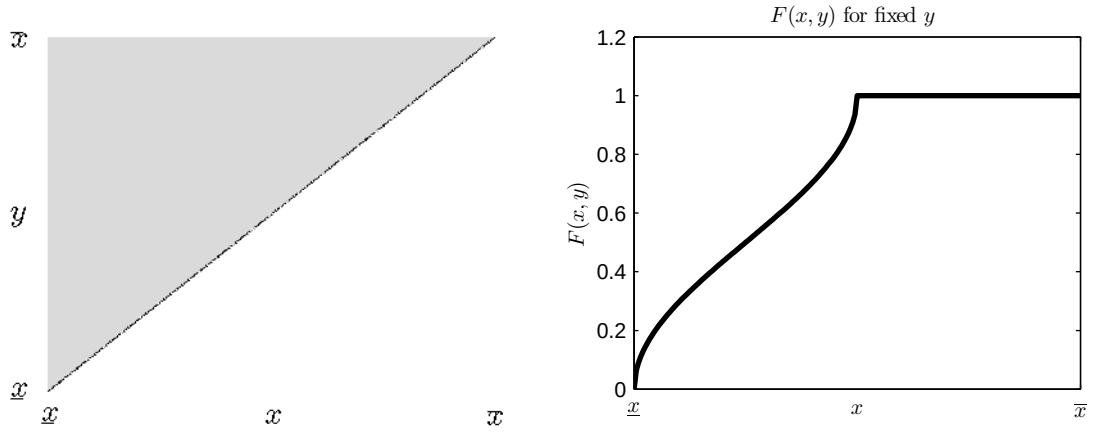

Figure 3.3.1: (a) Domain for the probability measure $F(x, y)$ showing admissible values for $F(x, y) \subset \mathscr{P}(Q)$. (b) Example $F(x, y) \subset \mathscr{P}(Q)$ for fixed y. In this example, $y = (\overline{x} - \underline{x})/2$.

3.3.1 Theoretical framework

Let $Q = [\underline{x}, \overline{x}]$ and $\mathscr{P}(Q)$ be the space of all probability measures on $(Q, \mathscr{A})$, where $\mathscr{A}$ is the Borel σ-algebra on Q. Since we are primarily concerned with the system in (3.2.1)-(3.2.3), we restrict the space of probability distributions to those that can be solutions to our inverse problem. A fragmentation cannot result in a daughter floc larger than the original floc, therefore we consider the subset $\mathscr{P}_y(Q) \subset \mathscr{P}(Q)$ such that $F(x, y) \in \mathscr{P}_y(Q)$ if $F(x, y) \equiv 1$ for $x \geq y$ and $y \in Q$. We also restrict our solutions to piecewise absolutely continuous (PAC) functions with a finite number of discontinuities in x. An illustration of the domain and an example distribution are shown in Figure 3.3.1, where the upper left corner of the domain admits values of $F(x, y)$ between 0 and 1, and the lower right requires $F(x, y) \equiv 1$. We then define our space of solutions to the inverse problem as $F \in \mathscr{F}(Q \times Q)$, the space of all PAC functions with a finite number of discontinuities in x such that $F(x, y) \in \mathscr{P}_y(Q)$ for any fixed y. We will denote this space of solutions as simply $\mathscr{F}$ throughout the remaining work.

We define a metric on the space $\mathscr{F}$ to create a metric topology, and we accomplish this by making use of the well-known Prohorov metric. We recall the definition of the Prohorov

metric on $\mathscr{P}(Q)$ for any arbitrary complete metric space Q with metric $dist$. For any closed $E \subset Q$ and $\epsilon > 0$, we define the ϵ-neighborhood of E by

$$E^{\epsilon} = \{q \in Q | dist(\tilde{q}, q) < \epsilon, for some \tilde{q} \in E\}.$$

Then the Prohorov metric is the mapping $\rho_{Proh} : \mathscr{P}(Q) \times \mathscr{P}(Q) \to \mathbb{R}^{+}$ defined by for $F, \tilde{F} \in \mathscr{F}$ and fixed y, the Prohorov metric to denote the distance

$$\rho_{Proh}(P_1, P_2) = \inf \{\epsilon > 0 | P_1(E^{\epsilon}) \leq P_2(E) + \epsilon, E \text{closed}, E \in Q\}.$$

A full description of the Prohorov metric can be found in [14]. Convergence in the Prohorov metric is equivalent to weak convergence of measures, and we direct the interested reader to [37] (which summarizes its relationship to a variety of other metrics on probability measures).

We extend this concept to define the metric ρ on the space $\mathscr{F}$ by taking the supremum of ρ_{Proh} over all $y \in Q$:

$$\rho(F, \tilde{F}) = \sup_{y \in Q} \rho_{Proh}(F(\cdot, y), \tilde{F}(\cdot, y)).$$

Let $n_j(t_i)$ represent the number of flocculated biomasses with volume between x_{j-1} and x_j at time t_i. We assume the error in our data is normally distributed, and thus our inverse problem entails finding a minimizer of the least squares cost functional, defined as:

$$\min_{F \in \mathscr{F}(Q \times Q)} J(F; \mathbf{n}) = \min_{F \in \mathscr{F}(Q \times Q)} \sum_{i=1}^{N_t} \sum_{j=1}^{N_x} \left(\int_{x_{j-1}}^{x_j} b(t_i, x, F)\, dx \; - \; n_j(t_i) \right)^2 \tag{3.3.1}$$

where the data $\mathbf{n} \in \mathbb{R}^{N_x \times N_t}$ consists of the number of flocs in each of the N_x bins for floc volume at N_t time points, and b is the solution to Equations (3.2.1)-(3.2.3) corresponding to F. Since J may not have a unique minimizer, we denote a corresponding solution set of

probability distributions as $\mathscr{F}^*(\mathbf{n})$. We then define the distance between two such sets of solutions, $\mathscr{F}^*(\mathbf{n})$ and $\mathscr{F}^*(\tilde{\mathbf{n}})$ (for data $\mathbf{n}$ and $\tilde{\mathbf{n}}$) to be the well-known Hausdorf distance:

$$d_H(\mathscr{F}^*(\mathbf{n}), \mathscr{F}^*(\tilde{\mathbf{n}})) = \inf\{\rho(F, \tilde{F}) : \ F \in \mathscr{F}^*(\mathbf{n}), \ \tilde{F} \in \mathscr{F}^*(\tilde{\mathbf{n}})\},$$

(see [52] for a full definition).

We now consider the abstract evolution equation formulation of Equations (3.2.1)-(3.2.3):

$$\begin{aligned} b_t &= g(b, \phi) \\ b(0, \cdot) &= b_0(x) \end{aligned} \tag{3.3.2}$$

for $t \geq 0$, and $\phi \in \mathscr{F}$, $b_0(x)$, $b(t, \cdot) \in H = L^1(Q, \mathbb{R}^+)$, the space of integrable functions mapping a closed bounded subset of the positive reals, i.e., $Q \subset \mathbb{R}^+$, into $\mathbb{R}^+$. For comparison with (3.2.1)-(3.2.3), ϕ corresponds to the post-fragmentation distribution $F(x, y)$, and the operator $g : H \times \mathscr{F} \to H$ is defined as

$$g(b, \phi) = \mathcal{G}b + \mathcal{A}(b) + \mathcal{F}(b, \phi) \tag{3.3.3}$$

where $\mathcal{A}$ and $\mathcal{F}$ are defined as mappings $H \mapsto H$ such that $\mathcal{A}(b) = A(\cdot, b)$ and $\mathcal{F}(b, \phi) = F(\cdot, b; \phi)$, and the operator $\mathcal{G} : \text{dom}\mathcal{G} \subset H \to H$ is defined as

$$\mathcal{G}\psi = -\frac{\partial}{\partial x}(G(x)\psi),$$

with $\text{dom}\mathcal{G} = \{\psi \in H : \ \mathcal{G}\psi \in H^1(\underline{x}, \overline{x}), \ \lim_{x \to \overline{x}}(\mathcal{G}\psi)(x) = 0, \ (\mathcal{G}\psi)(\underline{x}) = 0\}$. The restrictions on the domain can be interpreted biologically to be a no-flux boundary condition on floc growth at the minimum floc size ($(\mathcal{G}\psi)(\underline{x}) = 0$), and "well-behaved" floc growth near the maximum floc size ($\lim_{x \to \overline{x}}(\mathcal{G}\psi)(x) = 0$). The existence and uniqueness of solutions to 3.3.2 have been established by Bortz, et al. [19]. The growth function G, aggregation kernel K_A,

and fragmentation kernel K_F are not the focus of this study and so will be considered fixed throughout the following work.

3.3.2 Inverse Problem

The following two lemmas are used to prove existence of solutions to the inverse problem in Equation 3.3.1. We use the well-known result that a continuous function on a compact metric space has a minimum, and thus the first lemma shows that $(\mathscr{F}, \rho)$ is a compact metric space and the second shows the continuous dependence of the solution b on the probability measure F.

For much of the following analysis, we require the operator g to satisfy a Lipschitz-type condition. We detail that condition in the following.

Condition 3.3.1. Let (b, ϕ), $(\tilde{b}, \tilde{\phi}) \in H \times \mathscr{F}$. For fixed t, the function $g : H \times \mathscr{F} \to H$ must satisfy

$$\left\| g(b, \phi) - g(\tilde{b}, \tilde{\phi}) \right\| \leq C \left\| b - \tilde{b} \right\| + \mathscr{T}(\phi, \tilde{\phi}),$$

where $C > 0$, and $\mathscr{T}(\phi, \tilde{\phi})$ is some function $\mathscr{T} : \mathscr{F} \times \mathscr{F} \to \mathbb{R}$ such that $\mathscr{T}(\phi, \tilde{\phi}) \to 0$ as $\rho(\phi, \tilde{\phi}) \to 0$.

We begin by proving that $(\mathscr{F}, \rho)$ as defined is a compact metric space.

Lemma 3.3.2. *$(\mathscr{F}, \rho)$ is a compact metric space.*

Proof. Consider a Cauchy sequence $\{F_n\} \in \mathscr{F}$. Then $\forall\, \epsilon > 0$, $\exists\, N$ such that $\forall\, n, m \geq N$,

$$\sup_{y \in Q} \rho_{Proh}(F_n(\cdot, y), F_m(\cdot, y)) < \epsilon.$$

It is easy to see we have a Cauchy sequence $\{F_n(\cdot, y)\} \in \mathscr{P}_y(Q)$ which converges uniformly in $y \in Q$. From results in Billingsley [14], $\mathscr{P}_y(Q)$ is a compact metric space, so there exists $F(\cdot, y) \in \mathscr{P}_y(Q)$ such that $\rho_{Proh}(F_n(\cdot, y), F(\cdot, y)) < \epsilon$ for all $n \geq N$. Thus

$$\sup_{y\in Q} \rho_{Proh}(F_n(\cdot,y), F(\cdot,y)) < \epsilon$$

and $(\mathscr{F},\rho)$ is a complete metric space. In addition, since $Q\times Q$ is compact and $0 \le F(x,y) \le 1$ for all $(x,y) \in Q\times Q$, $F \in \mathscr{F}$, $\mathscr{F}(Q\times Q)$ is totally bounded and therefore $(\mathscr{F},\rho)$ is a compact metric space. □

Now that we have established a compact metric space, it remains to show that the cost functional on that space is continuous with respect to the function F. It suffices to prove point-wise continuity.

Lemma 3.3.3. *If $t \in I = [0,t_f]$, $F \in \mathscr{F}$, and the operator g in* (3.3.2) *satisfies Condition 3.3.1, then the unique solution b to* (3.3.2) *is point-wise continuous at $F \in \mathscr{F}$.*

Proof. For b to be point-wise continuous at F, we need to show that $\|b(t,x,F_i) - b(t,x,F)\| \to 0$ as $\rho(F_i,F) \to 0$ for $\{F_i\} \in \mathscr{F}$ and fixed t. We begin by re-writing (3.3.2) as an integral equation:

$$b(t,x) = b_0(x) + \int_0^t g(b(s,x),F)ds$$

For fixed t, consider b to be a function of F:

$$b(t,x,F) = b_0(x) + \int_0^t g(b(s,x,F),F)ds$$

By definition of solutions, we have:

$$\|b(t,\cdot,F_i) - b(t,\cdot,F)\| \le \int_0^t \|g(b(s,\cdot,F_i),F_i) - g(b(s,\cdot,F),F)\|\, ds$$

Based on the assumption on g, we obtain:

$$\|b(t,\cdot,F_i) - b(t,\cdot,F)\| \le C\int_0^t \|b(s,\cdot,F_i) - b(s,\cdot,F)\|\, ds + \mathcal{T}(F_i,F)$$

where we define $\mathcal{T}(F_i, F) = \int_0^{t_f} \mathscr{T}(F_i, F)ds$, independent of t. An application of Gronwall's inequality yields:

$$\|b(t, \cdot, F_i) - b(t, \cdot, F)\| \leq \mathcal{T}(F_i, F)\, e^{\int_0^t C\, ds} \leq \mathcal{T}(F_i, F)\, e^{C\, t_f} \to 0$$

since we know that $\mathcal{T}(F_i, F) \to 0$ as $F_i \to F$. Thus the solutions b are point-wise continuous at $F \in \mathscr{F}$. □

We use the results of the above two lemmas to establish existence of a solution to our inverse problem.

Theorem 3.3.4. *There exists a solution to the inverse problem as described in* (3.3.1)*.*

Proof. It is well known that a continuous function on a compact set obtains both a maximum and a minimum. We have shown $(\mathscr{F}, \rho)$ is compact, and from Lemma 3.3.3, for fixed t, we have that $F \mapsto b(t, \cdot, F)$ is continuous. Therefore J is continuous with respect to F and we can conclude there exist minimizers for J. □

3.4 Approximation of Solutions

Since the original problem involves minimizing over infinite dimensional space $\mathscr{F}$, pursuing this optimization is challenging without some type of finite dimensional approximation. Thus we define some approximation spaces over which the optimization problem becomes computationally tractable. Based on a discretization scheme presented in [12], let $Q_M = \{q_j^M\}_{j=1}^M$ be partitions of $Q = [\underline{x}, \overline{x}]$ for $M = 1, 2, \ldots$ and

$$Q_D = \bigcup_{M=1}^{\infty} Q_M \tag{3.4.1}$$

where the sequences are chosen such that Q_D is dense in Q.

For positive integers M, L, let the approximation space be defined as

$$\mathscr{F}^{ML} = \left\{ F \in \mathscr{F} \mid F(x,y) = \sum_{\ell=1}^{L} \sum_{m=1}^{M} p_{m\ell} \Delta_{q_m^M}(x)\, \Delta_{q_\ell^L}(y), \right. \\ \left. q_m^M \in Q_M,\, q_\ell^L \in Q_L,\, \sum_{m=1}^{\ell} p_{m\ell} = 1,\, i = 1, 2, \ldots, L \right\}$$

where Δ_q is the Heaviside step function with atom q. That is, $\Delta_q(x)$ is 1 if $x \geq q$ and 0 if $x < q$. Define

$$\mathscr{F}_D = \bigcup_{M,L=1}^{\infty} \mathscr{F}^{ML}.$$

Q is a complete, separable metric space, and by Theorem 3.1 in [11] and properties of the sup norm, $\mathscr{F}_D$ is dense in $\mathscr{F}$ in the ρ metric. Therefore we can directly conclude that any function $F \in \mathscr{F}$ can be approximated by a sequence $\{F_{M_j L_k}\}$, $F_{M_j L_k} \in \mathscr{F}^{M_j L_k}$ such that as $M_j,\, L_k \to \infty$, $\rho(F_{M_j L_k},\, F) \to 0$.

Similar to the discussion concerning Theorem 4.1 in [11], we now state the theorem regarding the continuous dependence of the inverse problem upon the given data, as well as stability under approximation of the inverse problem solution space $\mathscr{F}$.

Theorem 3.4.1. *Let $Q = [\underline{x}, \overline{x}]$, assume that for fixed $t \in [0, t_f]$, $x \in Q$, $F \mapsto b(t, x, F)$ is continuous on $\mathscr{F}$, and let Q_D be a countable dense subset of Q as defined in Equation 3.4.1. Suppose that the observed data $\mathbf{n}_m$, $\mathbf{n} \in \mathbb{R}^{N_t \times N_x}$ are such that $\mathbf{n}_m \to \mathbf{n}$ as $m \to \infty$. Moreover, suppose that $\mathscr{F}^{*ML}(\mathbf{n}_m)$ is the set of minimizers for $J(F; \mathbf{n}_m)$ over $F \in \mathscr{F}^{ML}$ corresponding to the data $\mathbf{n}_m$. Similarly, suppose that $\mathscr{F}^*(\mathbf{n})$ is the set of minimizers for $J(F; \mathbf{n})$ over $F \in \mathscr{F}$ corresponding to the data $\mathbf{n}$. Then, $d_H(\mathscr{F}^{*ML}(\mathbf{n}_m), \mathscr{F}^*(\mathbf{n})) \to 0$ as $M,\, L,\, m \to \infty$.*

Proof. Using continuous dependence of solutions on F, compactness of $(\mathscr{F}, \rho)$, and the density of $\mathscr{F}_D$ in $\mathscr{F}$, the arguments follow precisely those for Theorem 4.1 in [11], which would argue in the present context that any sequence $F_m^{*ML} \in \mathscr{F}^{*ML}(\mathbf{n}_m)$ has a subsequence $F_{m_k}^{*M_j L_i}$ that converges to a $\tilde{F} \in \mathscr{F}^*(\mathbf{n})$. Therefore we can claim that

$$d_H\left(\mathscr{F}^{*ML}(\mathbf{n}_m),\, \mathscr{F}^*(\mathbf{n})\right) = \inf\left\{\rho(F_m^{ML}, F) \mid F_m^{ML} \in \mathscr{F}^{*ML}(\mathbf{n}_m),\ F \in \mathscr{F}^*(\mathbf{n})\right\}$$

converges to zero as M, L, $m \to \infty$. □

Since we do not have direct access to an analytical solution to (3.3.2), our efforts are focused on the solving the approximate inverse problem

$$\min_{F\in\mathcal{F}} J^N(F, \mathbf{n}) = \min_{f\in\mathcal{F}} \sum_{i=1}^{N_t}\sum_{j=1}^{N_x}\left(\int_{x_{j-1}}^{x_j} b^N(t_i, x, F)dx - n_j(t_i)\right)^2 \tag{3.4.2}$$

with N_t data observations and N_x data bins for floc volume. From results in [19], we can obtain semi-discrete solutions b^N to the forward problem that converge uniformly in norm to the unique solution of (3.2.1)-(3.2.3) on a bounded time interval as $N \to \infty$. We summarize the framework and results for this approximation to the forward problem here for completeness.

We first form an approximation to H. We define basis elements

$$\beta_i^N(x) = \begin{cases} 1; & x_{i-1}^N \le x \le x_i^N \\ 0; & \text{otherwise} \end{cases} \qquad i = 1, \ldots, N,$$

for positive integer N and $\{x_i^N\}_{i=0}^N$ a partition of $[\underline{x}, \overline{x}]$ with largest mesh size Δx and $\Delta x_j = x_j - x_{j-1}$. These functions form an orthogonal basis for the approximate solution space

$$H^N = \left\{h \in H \mid h = \sum_{i=1}^N \alpha_i \beta_i^N,\ \alpha_i \in \mathbb{R}\right\},$$

and accordingly, we define the orthogonal projections $\pi^N : H \mapsto H^N$

$$\pi^N h = \sum_{j=1}^N \alpha_j \beta_j^N, \qquad \text{where } \alpha_j = \frac{1}{\Delta x_j}\int_{x_{j-1}^N}^{x_j^N} h(x)\, dx.$$

Finally we define the approximating operators $\mathcal{G}^N : H^N \to H^N$ of the infinitesimal operator by

$$\left(\mathcal{G}^N h\right)(x) = -\sum_{j=1}^{N} \frac{1}{\Delta x_j} \left(G(x_{j-1}^N)h(x_{j-1}^N) - G(x_j^N)h(x_j^N)\right) \beta_j^N(x),$$

for $h \in H^N$. Thus our approximating formulations of (3.2.1), (3.2.3) becomes the following system of N ODEs for $b^N \in H^N$

$$b_t^N = \mathcal{G}^N b^N + \pi^N(\mathcal{A}(b^N) + \mathcal{F}(b^N, \phi)), \tag{3.4.3}$$

$$b^N(0,x) = \pi^N b_0(x). \tag{3.4.4}$$

By results of Section 4 in [2], we know the semi-discrete solutions to 3.4.3 converge uniformly in norm to the unique solution of 3.2.1 on a bounded time interval as $N \to \infty$.

To have general "method stability" [13], we also need to show that $b^N(t,x,F_i) \to b(t,x,F)$ as $F_i \to F$ in the ρ metric and as $N \to \infty$. First, arguments similar to those in Lemma 3.3.3 can be used to show b^N is continuous in F on $\mathscr{F}$ for fixed N. Additionally, the convergence of $b^N(t,x,F_i) \to b^N(t,x,F)$ as N, $i \to \infty$ is shown.

Lemma 3.4.2. *Let $t \in I$, $F \in \mathscr{F}$,and $\{F_i\} \in \mathscr{F}$ such that $\lim_{i\to\infty} \rho(F_i, F) = 0$. For fixed N, if $b^N(t,x,F_i)$ is the solution to Equations* (3.4.3)-(3.4.4)*, then $\left\|b^N(t,\cdot,F_i) - b^N(t,\cdot,F)\right\| \to 0$ as $i \to \infty$ uniformly in t on I.*

Proof. For fixed N, we find that for $t \in [0,\, t_f]$

$$\begin{aligned}\left\|b^N(t,\cdot,F_i) - b^N(t,\cdot,F)\right\| \leq & \int_0^t \left\|\mathcal{G}^N b^N(s,\cdot,F_i) - \mathcal{G}^N b^N(s,\cdot,F)\right\| ds \\ & + \int_0^t \Big\|\pi^N \left(\mathcal{A}(b^N(s,\cdot,F_i)) + \mathcal{F}(b^N(s,\cdot,F_i),F_i)\right. \\ & \qquad \left. -\mathcal{A}(b^N(s,\cdot,F)) - \mathcal{F}(b^N(s,\cdot,F),F)\right)\Big\| ds.\end{aligned}$$

By definition of $\mathcal{G}^N b^N$,

$$\begin{aligned}\left\|\mathcal{G}^N b^N(t,\cdot,F_i) - \mathcal{G}^N b^N(t,\cdot,F)\right\| &\leq \sum_{j=1}^{N} \left\| \frac{1}{\Delta x_j} \|G\|_\infty \left[\left(b^N(t,x_{j-1}^N,F_i) - b^N(t,x_{j-1}^N,F)\right) \right.\right. \\ &\qquad \left.\left. - \left(b^N(t,x_j^N,F_i) - b^N(t,x_j^N,F)\right) \right] \beta_j^N(\cdot) \right\| \\ &\leq C_G \left\| b^N(t,\cdot,F_i) - b^N(t,\cdot,F) \right\|\end{aligned}$$

where $C_G = \frac{2\|G\|_\infty \bar{B}}{\min_j \Delta x_j}$ and $\overline{B} = \sup_{t\in I} \left\| b^N(t,\cdot,F_i) - b^N(t,\cdot,F) \right\|$. Also,

$$\left\| \pi^N \left(\mathcal{A}(b^N(t,\cdot,F_i)) + \mathcal{F}(b^N(t,\cdot,F_i),F_i) - \mathcal{A}(b^N(t,\cdot,F)) - \mathcal{F}(b^N(t,\cdot,F),F) \right) \right\|$$

$$\begin{aligned}&\leq \pi^N \left\| g(b^N(t,\cdot,F_i),F_i) - g(b^N(t,\cdot,F),F) \right\| \\ &\leq \pi^N \left(C \left\| b^N(t,\cdot,F_i) - b^N(t,\cdot,F) \right\| + \mathscr{T}(F_i,F) \right) \\ &\leq C\,\bar{B} \left\| b^N(t,\cdot,F_i) - b^N(t,\cdot,F) \right\| + \pi^N \mathscr{T}(F_i,F).\end{aligned}$$

Combining these results,

$$\left\| b^N(t,\cdot,F_i) - b^N(t,\cdot,F) \right\| \leq \int_0^t \tilde{C} \left\| b^N(t,\cdot,F_i) - b^N(t,\cdot,F) \right\| ds + \mathcal{T}^N(F_i,F)$$

where we define $\mathcal{T}^N(F_i,F) = \int_0^{t_f} \pi^N \mathscr{T}(F_i,F) ds$, independent of t, and $\tilde{C} = \frac{2\|G\|_\infty \bar{B}}{\min_j \Delta x_j} + C\,\bar{B}$. An application of Gronwall's inequality yields:

$$\left\| b^N(t,\cdot,F_i) - b^N(t,\cdot,F) \right\| \leq \mathcal{T}^N(F_i,F)\, e^{\int_0^t \tilde{C}\, ds} \leq \mathcal{T}^N(F_i,F)\, e^{\tilde{C}\, t_f} \to 0$$

since we know that $\mathcal{T}^N(F_i,F) \to 0$ as $F_i \to F$. Thus the solutions b^N are point-wise continuous at $F \in \mathscr{F}$. □

Corollary 3.4.3. *Under the conditions in Lemma 3.4.2, we can conclude that* $\left\| b^N(t,\cdot,F_N) - b(t,\cdot,F) \right\| \to 0$ *as* $N \to \infty$ *uniformly in* t *on* I.

Proof. Consider

$$\left\|b^N(t,\cdot,F_N) - b(t,\cdot,F)\right\| \leq \left\|b^N(t,\cdot,F_N) - b^N(t,\cdot,F)\right\| + \left\|b^N(t,\cdot,F) - b(t,\cdot,F)\right\|.$$

The first term converges by Lemma 3.4.2, while the second term converges as a result of the numerical scheme presented in [19]. □

With this corollary, we now consider the existence of a solution to the approximate inverse problem in Equation (3.4.2), as well as the solution's dependence on the given data **n**.

Theorem 3.4.4. *There exists solutions to both the original and approximate inverse problems in Equations* (3.3.1) *and* (3.4.2)*, respectively. Moreover, one can find solutions to the family of problems in Equation* (3.4.2) *that converge to a solution of Equation* (3.3.1) *as* $N \to \infty$.

Proof. As noted above, $(\mathscr{F}, \rho)$ is compact. By Lemmas 3.3.3 and 3.4.2, we have that both $F \mapsto b(t,\cdot,F)$ and $F \mapsto b^N(t,\cdot,F)$, for fixed $t \in [0,t_f]$, are continuous with respect to F. We therefore know there exist minimizers in $\mathscr{F}$ to the original and approximate cost functionals J and J^N respectively.

Let $\{F_N^*\} \in \mathscr{F}$ be any sequence of solutions to (3.4.2) and $\{F_{N_k}^*\}$ a convergent (in ρ) subsequence of minimizers. Recall that minimizers are not necessarily unique, but one can always select a convergent subsequence of minimizers in $\mathscr{F}$. Denote the limit of this subsequence F^*. By the minimizing properties of $F_{N_k}^* \in \mathscr{F}$, we then know that

$$J^{N_k}(F_{N_k}^*) \leq J^{N_k}(F) \qquad \text{for all } F \in \mathscr{F}. \tag{3.4.5}$$

By Corollary 3.4.3, we have the convergence of $b^N(t,\cdot,F_N) \to b(t,\cdot,F)$ and thus $J^N(F_N) \to J(F)$ as $N \to \infty$ when $\rho(F_N,F) \to 0$. Thus in the limit as $N_k \to \infty$, the inequality in (3.4.5) becomes

$$J(F^*) \leq J(F) \qquad \text{for all } F \in \mathscr{F}$$

with F^* providing a (not necessarily unique) minimizer of (3.3.1). □

Theorem 3.4.5. *Assume that for fixed $t \in [0, t_f]$, $F \mapsto b(t, \cdot, F)$ is continuous on $\mathscr{F}$ in ρ, b^N is the approximate solution to the forward problem given Equations* (3.4.3)-(3.4.4)*, J^N is the approximation given in* (3.4.2)*, and let Q_D be a countable dense subset of Q as defined in Equation* (3.4.1)*. Suppose that the observed data $\mathbf{n}_m$, $\mathbf{n} \in \mathbb{R}^{M_t \times M_x}$ are such that $\mathbf{n}_m \to \mathbf{n}$ as $m \to \infty$. Moreover, suppose that $\mathscr{F}_N^{*ML}(\mathbf{n}_m)$ is the set of minimizers for $J^N(F; \mathbf{n}_m)$ over $F \in \mathscr{F}^{ML}$ corresponding to the data $\mathbf{n}_m$. Similarly, suppose that $\mathscr{F}^*(\mathbf{n})$ is the set of minimizers for $J(F; \mathbf{n})$ over $F \in \mathscr{F}$ corresponding to the data $\mathbf{n}$. Then, $d_H(\mathscr{F}_N^{*ML}(\mathbf{n}_m), \mathscr{F}^*(\mathbf{n})) \to 0$ as N, M, L, $m \to \infty$.*

Proof. If we combine the arguments of Theorem 3.4.1, Theorem 3.4.4, and Corollary 3.4.3, as in Theorem 4.1 of [11], we readily obtain

$$d_H\left(\mathscr{F}_N^{*ML}(\mathbf{n}_m),\, \mathscr{F}^*(\mathbf{n})\right) = \inf\left\{\rho(F_{N,m}^{ML}, F) \mid F_{N,m}^{ML} \in \mathscr{F}_N^{*ML}(\mathbf{n}_m),\ F \in \mathscr{F}^*(\mathbf{n})\right\}$$

as N, M, L, $m \to \infty$. □

With the results of these two theorems, we can claim that both there exists a solution to the inverse problem and it is continuously dependent on the given data. We have established method stability under approximation of the state space and parameter space of our inverse problem, and well-posedness of the forward problem was established in [19]. Therefore we can conclude general well-posedness of the inverse problem.

3.5 Example Illustration

We now consider the application of this framework to the system in (3.2.1)-(3.2.3). For fixed $t \in I, b(t, \cdot) \in H$, $\phi \in \mathscr{F}$, consider the right side of (3.2.1), represented by (3.3.3),

$$g(b,\phi) = \mathcal{G}b + \mathcal{A}(b) + \mathcal{F}(b,\phi)$$

Claim 3.5.1. The function g satisfies Condition 3.3.1.

Proof. Consider

$$\begin{aligned}\left\|g(b,\phi) - g(\tilde{b},\tilde{\phi})\right\| &= \left\|(\mathcal{G}b - \mathcal{G}\tilde{b}) + (\mathcal{A}(b) - \mathcal{A}(\tilde{b})) + (\mathcal{F}(b,\phi) - \mathcal{F}(\tilde{b},\tilde{\phi}))\right\| \\ &\leq \left\|\mathcal{G}b - \mathcal{G}\tilde{b}\right\| + \left\|\mathcal{A}(b) - \mathcal{A}(\tilde{b})\right\| + \left\|\mathcal{F}(b,\phi) - \mathcal{F}(\tilde{b},\tilde{\phi})\right\|\end{aligned}$$

It is straightforward to show that both $\mathcal{G}b$ and $\mathcal{A}(b)$ are Lipschitz in b (see the proof of Lemma 3.1 in [2] for an illustration) with Lipschitz constants C_{growth} and C_{agg}, respectively. Examining the fragmentation term, we find

$$\begin{aligned}\left\|\mathcal{F}(b,\phi) - \mathcal{F}(\tilde{b},\tilde{\phi})\right\| &\leq \left\|\frac{1}{2}K_F(\cdot)\left(\tilde{b}(t,\cdot) - b(t,\cdot)\right)\right\| \\ &\quad + \left\|\int_{\cdot}^{\overline{x}} K_F(y)\left(b(t,y)\,\Gamma(\cdot,y) - \tilde{b}(t,y)\,\tilde{\Gamma}(\cdot,y)\right)dy\right\| \\ &\leq \frac{1}{2}K\left\|b - \tilde{b}\right\| + K\left\|\int_Q b(t,y)\left(\Gamma(\cdot,y) - \tilde{\Gamma}(\cdot,y)\right)dy\right\| \\ &\quad + K\left\|\int_Q \left(b(t,y) - \tilde{b}(t,y)\right)\tilde{\Gamma}(\cdot,y)\,dy\right\|\end{aligned}$$

where $K = \|K_F\|_\infty$. Examining the second term on the right hand side,

$$\begin{aligned}\left\|\int_Q b(t,y)\left(\Gamma(\cdot,y) - \tilde{\Gamma}(\cdot,y)\right)dy\right\| &\leq \int_Q\int_Q |b(t,y)|\left|\Gamma(x,y) - \tilde{\Gamma}(x,y)\right|dy\,dx \\ &\leq \int_Q |b(t,y)|\int_Q \left|\Gamma(x,y)dx - \tilde{\Gamma}(x,y)dx\right|dy \\ &\leq \int_Q |b(t,y)|\left(\int_Q \left|d\phi_y - d\tilde{\phi}_y\right|\right)dy.\end{aligned}$$

Since $\int_Q \left|d\phi_y - d\tilde{\phi}_y\right| \to 0$ is equivalent to $\rho_{Proh}(\phi_y, \tilde{\phi}_y) \to 0$, we know that

$$\sup_{y\in Q}\int_Q \left|d\phi_y - d\tilde{\phi}_y\right| \to 0 \quad \text{as} \quad \rho(\phi,\tilde{\phi}) \to 0.$$

We are integrating over a compact domain, and therefore

$$\left\|\int_Q b(t,y)\left(\Gamma(\cdot,y) - \tilde{\Gamma}(\cdot,y)\right)dy\right\| \to 0 \quad \text{as} \quad \rho(\phi,\tilde{\phi}) \to 0.$$

Similar analysis for the third term leads to the bound

$$\left\|\int_Q \left(b(t,y) - \tilde{b}(t,y)\right)\tilde{\Gamma}(\cdot,y)\,dy\right\| \leq K\left\|b-\tilde{b}\right\|.$$

Combining, we find the overall fragmentation term can be bounded by

$$\left\|\mathcal{F}(b,\phi) - \mathcal{F}(\tilde{b},\tilde{\phi})\right\| \leq \frac{3}{2}K\left\|b-\tilde{b}\right\| + \mathscr{T}(\phi,\tilde{\phi}).$$

Using the Lipschitz constants from the growth and aggregation terms,

$$\left\|g(b,\phi) - g(\tilde{b},\tilde{\phi})\right\| \leq C\left\|b-\tilde{b}\right\| + \mathscr{T}(\phi,\tilde{\phi})$$

where $C = \frac{3}{2}K + C_{growth} + C_{agg}$. □

Therefore, since the function g satisfies Condition 3.3.1, we can conclude well-posedness of the inverse problem for identifying the post-fragmentation probability density, $\Gamma(x,y)$, found in the model for flocculation dynamics of bacterial aggregates described in Equation (3.2.1)-(3.2.3).

3.6 Concluding Remarks

Our efforts here are motivated by a class of mathematical models which characterize a random process, such as fragmentation, by a probability distribution. We are concerned with the inverse problem for inferring the probability distribution, and we present the specific problem for the flocculation dynamics of aggregates in suspension which motivated this

study. We then developed the mathematical framework in which we establish well-posedness of the inverse problem for inferring the probability distribution. We also include results for overall method stability for numerical approximation, confirming a computationally feasible methodology. Finally, we verify that our motivating example in flocculation dynamics conforms to the developed framework.

CHAPTER 4

NUMERICAL SIMULATIONS FOR INFERRING THE POST-FRAGMENTATION DENSITY

4.1 Introduction

The previous chapter developed the necessary framework for showing the well-posedness of the inverse problem for finding conditional probability measures in a class of measure-dependent partial differential equations (PDE). We now focus on the system of PDE for flocculation dynamics of suspended bacterial aggregates, presented originally in [19] and used throughout this document.

The theory surrounding the inverse problem as developed in Chapter 3 is the foundation for ensuring computed solutions are viable, however the computational robustness and sensitivity of the proposed numerical scheme for finding these solutions must be investigated further to verify the utility of the approach. In this chapter we present a series of numerical simulations that explore the scheme proposed in the previous chapter. We summarize this scheme for the inverse problem for finding the post-fragmentation density in the system described in Section 3.2.

When parameter inference is conducted in aggregation-fragmentation models, we typically find it being used in the inference of the growth rate, fragmentation rate, and/or aggregation rate, and these rates are usually assumed to be constant. Examples of this type of parameter inference can be found in [1, 19]. When inferring a distribution, it is common to find that distribution parameterized in some way (e.g. a normal distribution parameterized

by its mean and variance), where only the parameters are fitted (e.g. [94, 5]). In contrast, the work presented here uses a nonparametric distribution and infers the function values for a discretization of the distribution (see [25] for more information on nonparametric distributions). This approach allows more freedom in the inference of the distribution by not assuming **a priori** a particular functional form, and in doing so provides stronger evidence to support the validity of the fitted distribution.

When any parameter inference is being conducted, it is natural to want to understand how changes in the parameters affect the model solution. One way to address this concern is to perform a **sensitivity analysis**. Developed in the context of modern control theory, the sensitivity equations are often used in optimization and inverse problems [88, 77]. The solution to these equations contain information regarding the sensitivity of our original system to changes in a particular parameter. Again, in this investigation the focus is not on a single parameter but a non-parameterized function, and the sensitivity analysis is adapted accordingly.

In section 4.2 we present the numerical scheme for solving the forward problem and its implementation, as well as summarize the approximation to the inverse problem as first presented in the previous chapter. In Section 4.3, we explore the robustness of the proposed scheme to noise in the data as well as its accuracy in connection with the mesh size employed. Section 4.4 examines the **sensitivity equations** associated with the population density model and addresses the experimental considerations concerning the times and floc sizes for data acquisition most important for

4.2 Background

Since we do not have access to the analytical solution to the system (3.2.1)-(3.2.3), we consider instead the approximate problem detailed in [19] and outlined in Section 3.4. We summarize here the approximate forward and inverse problems, and include additional detail on the numerical implementation.

Results in [19] show convergence of semi-discrete solutions b^N to the forward problem that converge uniformly in norm to the unique solution of (3.2.1)-(3.2.3) on a bounded time interval as $N \to \infty$. Our approximating formulations of (3.2.1)-(3.2.3) becomes the following system of N ODEs

$$b_t^N = \mathcal{G}^N b^N + \pi^N(\mathcal{A}(b^N) + \mathcal{F}(b^N, \phi)), \tag{4.2.1}$$

$$b^N(0,x) = \pi^N b_0(x). \tag{4.2.2}$$

where $\pi^N h$ is the projection operator of a function $h \in H = L^1[\underline{x}, \overline{x}]$ to the approximation space

$$H^N = \left\{ h \in H : \, h = \sum_{i=1}^{N} \alpha_i \beta_i^N, \, \alpha_i \in \mathbb{R} \right\}$$

and the basis elements β_i^N are defined as

$$\beta_i^N(x) = \begin{cases} 1; & x_{i-1}^N \le x \le x_i^N \\ 0; & \text{otherwise} \end{cases} \qquad i = 1, \ldots, N.$$

$\mathcal{G}^N b^N$, $\pi^N \mathcal{A}(b^N)$, and $\pi^N \mathcal{F}(b^N)$ are the projection of the growth, aggregation, and fragmentation functions (as defined in Section 3.4) to our basis elements. The resulting functions were discretized and implemented as the following approximating matrices. The matrix representation of $\mathcal{G}^N$ is given by

$$\left[G^N\right] = \begin{bmatrix} -\frac{1}{\Delta x_1} G(x_1^N) & 0 & 0 & \cdots & 0 \\ \frac{1}{\Delta x_1} G(x_1^N) & -\frac{1}{\Delta x_2} G(x_2^N) & 0 & \ddots & 0 \\ 0 & \ddots & \ddots & 0 & \vdots \\ \vdots & \ddots & \frac{1}{\Delta x_{N-2}} G(x_{N-2}^N) & -\frac{1}{\Delta x_{N-1}} G(x_{N-1}^N) & 0 \\ 0 & \cdots & 0 & \frac{1}{\Delta x_{N-1}} G(x_{N-1}^N) & -\frac{1}{\Delta x_N} G(x_N^N) \end{bmatrix}. \tag{4.2.3}$$

The application of π^N to $\mathcal{A}^N(b)$ is

$$\left[\pi^N \mathcal{A}(b^N)\right] = \begin{bmatrix} -\alpha_1 \sum_{j=1}^{N-1} K_A(x_1, x_j)\alpha_j \Delta x_j \\ \frac{1}{2} K_A(x_1, x_1)\alpha_1 \alpha_1 \Delta x_1 - \alpha_2 \sum_{j=1}^{N-2} K_A(x_2, x_j)\alpha_j \Delta x_j \\ \vdots \\ \frac{1}{2} \sum_{j=1}^{N-2} K_A(x_j, x_{N-1-j})\alpha_j \alpha_{N-1-j} \Delta x_j - \alpha_{N-1} K_A(x_{N-1}, x_1)\alpha_1 \Delta x_1 \\ \frac{1}{2} \sum_{j=1}^{N-1} K_A(x_j, x_{N-j})\alpha_j \alpha_{N-j} \Delta x_j \end{bmatrix} \tag{4.2.4}$$

and the application of π^N to $\mathcal{F}^N(b)$ is

$$\left[\pi^N \mathcal{F}(b^N)\right] = \begin{bmatrix} \sum_{j=2}^{N} \Gamma(x_1, x_j) K_F(x_j)\alpha_j \Delta x_j \\ \sum_{j=3}^{N} \Gamma(x_2, x_j) K_F(x_j)\alpha_j \Delta x_j - \frac{1}{2} K_F(x_2)\alpha_2 \Delta x_2 \\ \vdots \\ \Gamma(x_{N-1}, x_N) K_F(x_N)\alpha_N \Delta x_N - \frac{1}{2} K_F(x_{N-1})\alpha_{N-1} \Delta x_{N-1} \\ -\frac{1}{2} K_F(x_N)\alpha_N \Delta x_N \end{bmatrix}. \tag{4.2.5}$$

The growth function $G(x)$ we used in our model is the standard logistic growth model

$$G(x) = \gamma_G \, x \, \left(1 - \frac{x}{\overline{x}}\right).$$

with growth rate γ_G. The aggregation kernel $K_A(x, y)$ used is the turbulent mixing model

$$K_A(x, y) = \gamma_A (\epsilon/\nu)^{1/2} \left(x^{1/3} + y^{1/3}\right)^3$$

where γ_A is the aggregation rate, ϵ is the rate of energy dissipation per unit mass and ν is the kinematic viscosity. The fragmentation kernel $K_F(x)$ was chosen to reflect the standard practice of proportionality to floc size and is given by

$$K_F(x) = \gamma_F (x - \underline{x})^{1/3}.$$

with fragmentation rate γ_F. For the constants γ_G, γ_A, and γ_F, as well as the initial condition $b_0(x)$ for solving the forward problem, we used the functions and values fitted to data from [19]. Table 4.1 is a summary of the parameters and functions common to all simulations.

Symbol	Value	Description	Units
γ_G	6.8×10^{-4}	Growth	min^{-1}
γ_A	2.7×10^{-15}	Aggregation	fL^{-2}
γ_F	6.6×10^{-5}	Fragmentation	μm^{-1} fL^{-1} min^{-1}
$b_0(x)$	$C_1 e^{\gamma_1 x} + C_2 e^{\gamma_2 x}$	Initial volume density	# flocs/fL
	$C_1 = 3.89 \times 10^9$, $\gamma_1 = -1.56$		
	$C_2 = 7.47 \times 10^{-4}$, $\gamma_2 = -0.00676$		

Table 4.1: Summary of parameters and functions common to all simulations.

The approximate inverse problem is given by

$$\min_{F \in \mathcal{F}} J^N(F, \mathbf{n}) = \min_{F \in \mathcal{F}} \sum_{i=1}^{N_t} \sum_{j=1}^{N_x} \left(\int_{x_{j-1}}^{x_j} b^N(t_i, x, F) dx - n_j(t_i) \right)^2 \tag{4.2.6}$$

where the data $\mathbf{n} \in \mathbb{R}^{N_x \times N_t}$ consists of the number of flocs in each of the N_x bins for floc volume at N_t time points, and b^N is the solution to Equations (4.2.1)-(4.2.2) corresponding to F.

4.3 Approximation of Solutions

Numerical simulations are used to demonstrate the utility and robustness of the approximation scheme presented. Simulated data were generated by solving the forward problem using the method from 4.2. The post-fragmentation density $\Gamma_{generating}(x, y)$ used to generate these data was derived from previous work [20] and is depicted in Figure 4.3.1. These data serve as the "observed" data $\mathbf{n}$ and correspond to the true solution $b^N(t, x, \Gamma)$ of approximate forward problem. All calculations were carried out using MATLAB routines.

Without loss of generality, we assume a spatial domain of $Q = [0, 1]$ and a temporal domain of $I = [0, 1]$. We discretized the interval $Q = [0, 1]$ into N intervals of length $\frac{1}{N}$, generating the partition $Q_N = q_j{}_{j=1}^{N} = \left\{ \frac{j}{N} \right\}_{j=1}^{N}$ where the q_j are the right endpoints of each subinterval. Note that $Q_D = \bigcup_{N=1}^{\infty} Q_N$ is a countable dense subset of Q. This spatial discretization also yields the matrix form of the post-fragmentation density, $\Gamma^N(q_j, q_k)$, $j, k = 1, \ldots, N$, and it is the elements of this matrix that form the parameter set for the

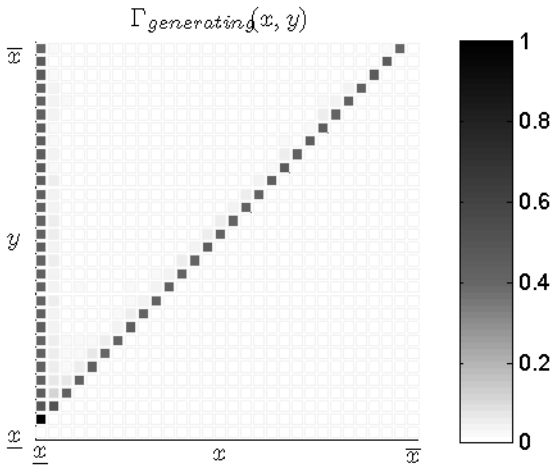

Figure 4.3.1: Post-fragmentation density $\Gamma_{generating}(x, y)$ used to generate test data for exploring the viability of the proposed numerical method for the inverse problem of inferring the post-fragmentation density function $\Gamma(x, y)$ from population data for flocculation dynamics.

optimization. The time interval $I = [0, 1]$ was discretized by $t_i = \frac{i}{N_t}$, $0 \leq i \leq N_t$, and the problem 4.2.1 was solved at each point $b(t_i, q_j)$.

Nonlinear constrained optimization was used to minimize the cost functional and implemented using the MATLAB `fmincon` function. The elements of $\Gamma^N(q_j, q_k)$ were required to be between the values of zero and one, as well as satisfy the constraint equation

$$\sum_{j=i}^{N} \Gamma^N(q_j, q_k) \;=\; 1 \qquad \text{for each } k$$

which guarantees the Γ^N is a probability density conditioned on y. Constraints of this type suggest that use of the MATLAB `active-set` algorithm for the optimization will be fruitful. An active set algorithm is a nonlinear constrained optimization algorithm typically used with inequality/equality type constraints, $g_i(x) \geq 0$. The name comes from the algorithm's internal classification of constraints as either active or inactive, where a constraint is inactive if $g_i(x) > 0$, and $g_i(x) = 0$ can be either active or inactive (depending on choice of active set). The algorithm uses a two stage approach: in the first stage active constraints are set as equality-type constraints and the constrained optimization problem is solved, and in the second stage the algorithm decides which constraints to activate and deactivate. For more details on active-set algorithms and constrained optimization, we direct the reader to the resources [67, 66, 39], though these listed represent only a small number of those available.

The size of the parameter set grows as N^2, and even the coarse discretization $N = 10$ yields an unwieldy 100 element set to optimize over. While there is no way around the problem of scaling, we addressed this issue in our implementation in two ways. First, since $\Gamma(x, y) \equiv 0$ for $x \geq y$, we only optimized over those elements of $\Gamma^N(q_j, q_k)$ where $j < k$ and let all other elements remain zero. Second, since the post-fragmentation density $\Gamma(x, y)$ models a single fragmentation event, the values of $\Gamma(x, y)$ were required to be symmetric with respect to daughter floc size ($\Gamma(x, y) = \Gamma(y - x, y)$) to reflect the symmetric nature of fragmentation. In our implementation, this constraint meant that the number of optimizable elements were

cut roughly in half. Combining the two constraints, the optimization for $N = 10$ was reduced from a 100 element set to a significantly more manageable 25 element set.

The algorithm was seeded with an initial density comprised of the uniform density in x for fixed y,

$$\Gamma_{uniform}(x,y) = \begin{cases} \frac{1}{y}; & 0 \leq x < y \\ 0; & x \geq y \end{cases}, \qquad x, y \in [0,1].$$

Our initial discretization uses $M = L = N_x = m = 30$, and the result of the optimization, $\Gamma_{optimized}(x,y)$, is shown in Figure 4.3.2. While this result is not identical to the generating density, it is very similar and displays the important feature of erosion. The success of this initial study serves as the foundation for further investigation into the robustness and accuracy of the approximation method.

4.3.1 Robustness to noise

Data gathered in the laboratory will by nature always include some level of noise due to any number of sources, such as measurement error or equipment precision. It is therefore important to examine the effect that noise in the data will have on the method's ability to determine the post-fragmentation density function. Using our baseline numerical solution $\mathbf{n}$, relative Gaussian noise was added creating "data" $\mathbf{n}_{\sigma^2}$, where the elements $n^{ij}_{\sigma^2}$ of $\mathbf{n}_{\sigma^2}$ are given by $n^{ij}_{\sigma^2} = n^{ij} + \epsilon^{ij}$ where the ϵ^{ij} are independent, identically-distributed Gaussian random variables with mean zero and variance σ^2 a scalar multiple of n^{ij}.

The value of the least squares cost functional J^N between the true solution $b^N(t,x,\Gamma)$ and the solution found using the optimized post-fragmentation density Γ_{fit} for each noise level is shown in Figure 4.3.3. As expected, the cost functional decreases in value with lower noise levels. The values appear to increase linearly with increased variance in the data, implying the error in the approximation due to normally distributed noise is of first-order.

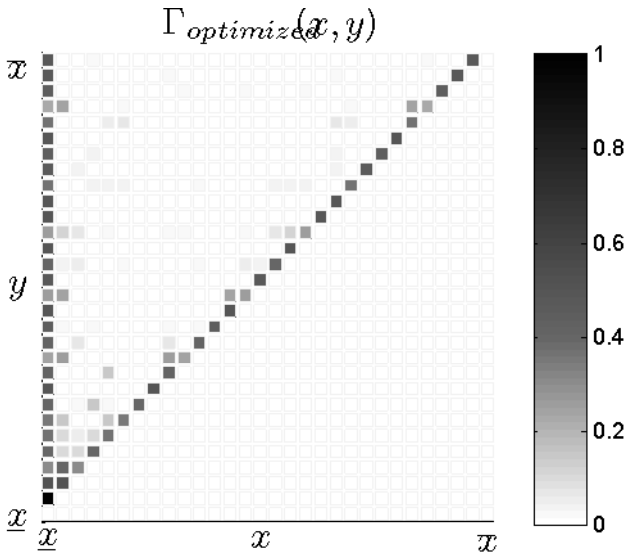

Figure 4.3.2: Preliminary evidence of the viability of the proposed numerical method for the inverse problem of inferring the post-fragmentation density function $\Gamma(x, y)$ from population data for flocculation dynamics. Shown is the fitted density function from the optimization scheme based on these data and an initial density function uniform in x, and it is qualitatively very similar to the generating density (shown in Figure 4.3.1).

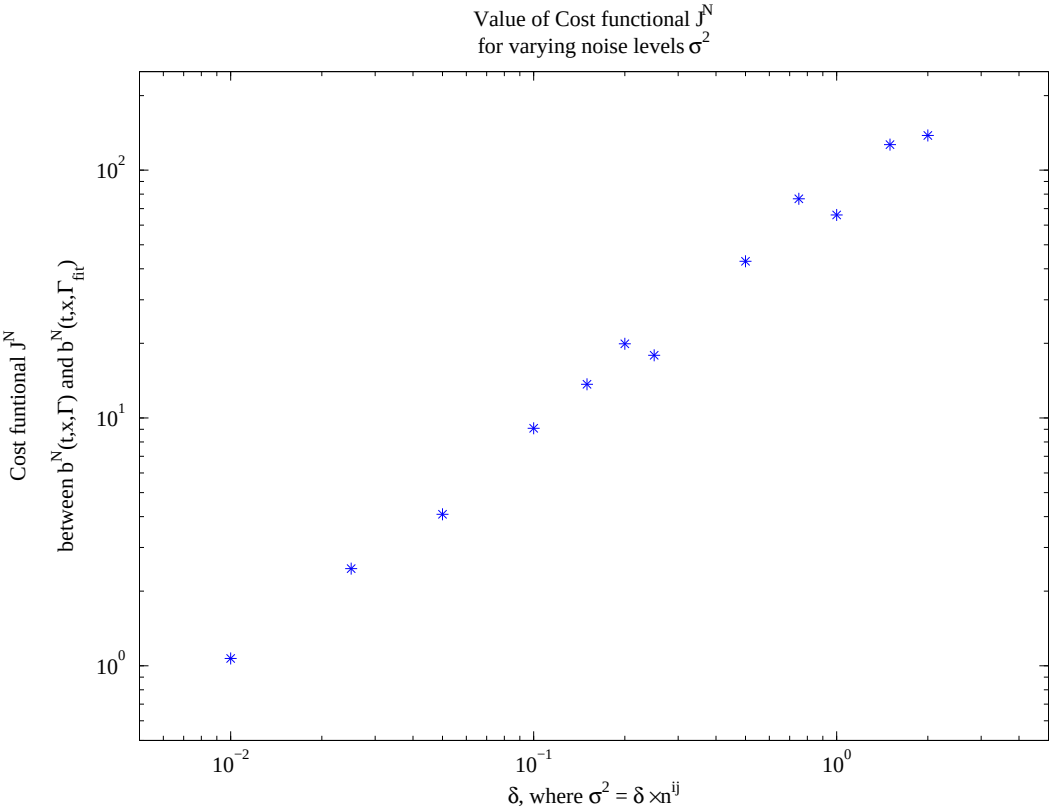

Figure 4.3.3: The robustness of the approximation method to varying levels of noise in the observed data. The value of the cost functional J^N for the optimized solution to the inverse problem is shown for data with relative Gaussian noise of mean zero and variance σ^2.

For the noise levels considered, the corresponding optimized post-fragmentation densities $\Gamma_{\sigma^2}(x, y)$ for two representative noise levels are shown in Figure 4.3.4. While the optimized density for low relative noise ($\sigma^2 = 0.025\, n^{ij}$) strongly resembles $\Gamma_{generating}$, the density for the high noise level of $\sigma^2 = 1.5\, n^{ij}$ is visibly different from $\Gamma_{generating}$ remaining similar to the seeded uniform density.

4.3.2 Effect of mesh size on accuracy

We next investigate the effect of mesh size on the accuracy of the optimization method. The interval $Q = [0, 1]$ was discretized into N subintervals of length $dx = 1/N$, with the number of subintervals increasing from $N = 5$ to $N = 50$. The value of the least squares cost functional J^N for the optimized solutions $\Gamma_{optimized}$ for each step size $dx = 1/N$ is shown in Figure 4.3.5.

As mentioned previously, a full discretization of $\Gamma(x, y)$ creates an $N \times N$ matrix $\Gamma^N(x^N, y^N)$ and since each element of the matrix is allowed to vary, the complexity of the optimization increases as N^2. We reduce the number of parameters in the optimization by considering only non-zero elements in the optimization scheme and enforcing the symmetry intrinsic in fragmentation. Examing the results presented in Figure 4.3.5, we see the expected improvement in accuracy with smaller step sizes regardless of the noise level. We also note an increase in the value of the least squares cost when the same analysis is carried out on data with more noise, but we still see improved accuracy of the numerical scheme with decreased stepsize.

4.4 Sensitivity analysis

It is natural to want to understand the sensitivity of the solution $b(t, x)$ of Equation (3.2.1) to changes in the post-fragmentation density $\Gamma(x, y)$. By examining this sensitivity, we gain information about where the solution is most affected by $\Gamma(x, y)$ and can use this information to aid in the design of future experiments. For more information on sensitivity

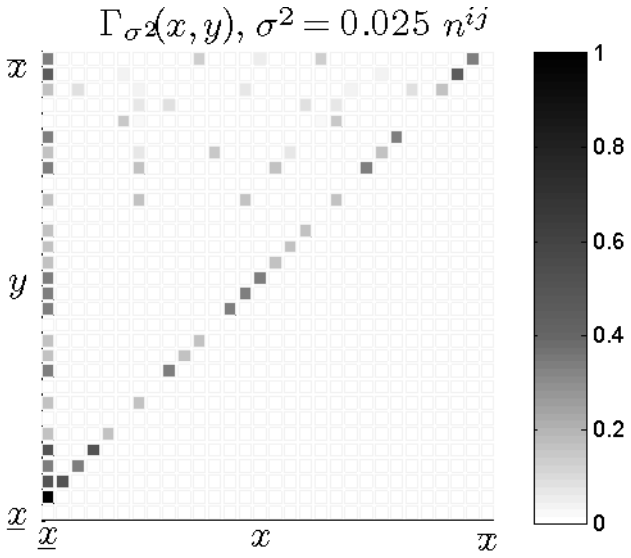

Figure 4.3.4: The optimized post-fragmentation density function Γ_{σ^2} for different levels of relative noise in the data. Gaussian noise was added to the true data n^{ij} to obtain noisy data of the form $n^{ij}_{\sigma^2} = n^{ij} + \epsilon^{ij}(n^{ij})$ where the ϵ^{ij} are normal random variable with mean 0 and variance $\sigma^2 = \delta n^{ij}$. (a) Low noise levels ($\delta = 0.025$) yield Γ_{σ^2} closely resembling the $\Gamma_{generating}$ used to create the true data. (b) Larger noise levels ($\delta = 1.5$) yield Γ_{σ^2} similar to the uniform density used to seed to optimization algorithm.

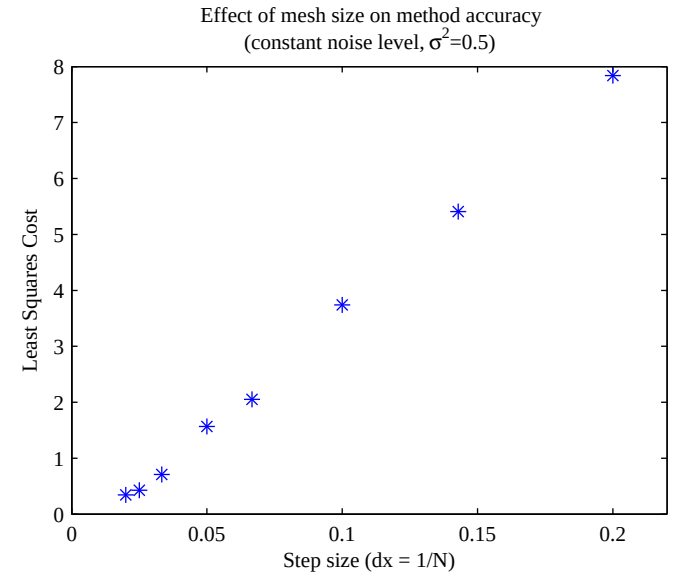

(a)

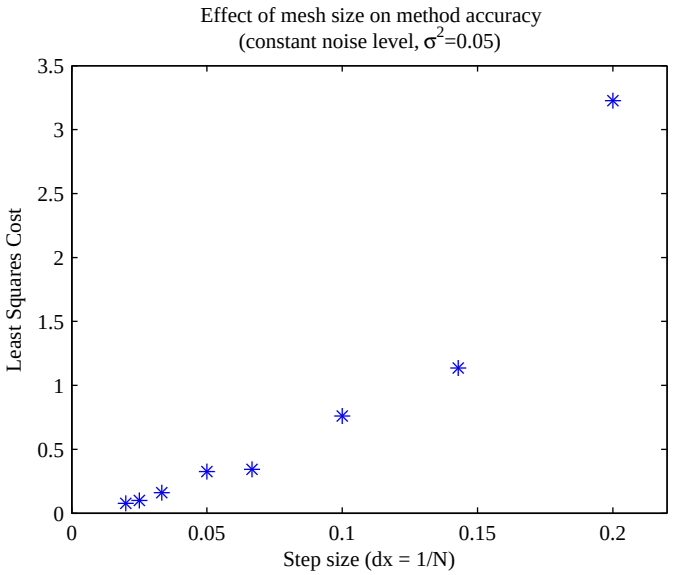

(b)

Figure 4.3.5: The robustness of the approximation method to different step sizes $dx = 1/N$ in the approximation scheme. Noise in the data was fixed at (a) $\sigma^2 = 0.05$ and (b) $\sigma^2 = 0.5$. The value of the cost functional J^N for the optimized solution to the inverse problem is shown for the number of grid points increasing from $N = 5$ to $N = 50$, with corresponding step sizes decreasing from $dx = 0.2$ to $dx = 0.02$.

theory, we direct the interested reader to the following texts [32, 97, 100, 30, 88].

4.4.1 Sensitivity equations

To perform this analysis, we must first derive the **sensitivity equations** [32, 30]. The solution to these equations contain information regarding the sensitivity of our original system to changes in a particular parameter. We find these by taking the derivative of with respect to Γ in the original PDE (Equations (3.2.1)-(3.2.3)). Because we are taking the derivative with respect to a function and not a parameter or variable, we make use of the **Gateaux derivative** [35, 36] commonly used in calculus of variations. The Gateaux derivative is a generalization of the concept of a directional derivative from vector calculus, where we now take the derivative in the direction of a function instead of a vector in $\mathbb{R}^N$. To define this functional derivative, consider X, Y Banach spaces, $W \subset X$ is open, and $F : X \to Y$. The Gateaux derivative $\frac{d}{d\psi}F(x;\psi)$ of F at $x \in W$ in the direction $\psi \in X$ is defined as

$$\frac{d}{d\psi}F(x;\psi) = \lim_{\tau \to 0} \frac{F(x+\tau\psi) - F(x)}{\tau},$$

noting that the derivative is a local derivative around the point x. The function F is called Gateaux differentiable at x if this limit exists for all $\psi \in X$. We formally apply this derivative to the PDE in Equations (3.2.1)-(3.2.3) and obtain our sensitivity equations.

$$\frac{\partial}{\partial\Gamma}\Big(\dot{b}(t,x,\Gamma) = -\left(G(x)b(t,x,\Gamma)\right)_x + A(x,b(t,x,\Gamma)) + F(x,b(t,x,\Gamma),\Gamma)\Big) \quad (4.4.1)$$

$$\frac{\partial}{\partial\Gamma}G(\underline{x})b(t,\underline{x},\Gamma) = 0, \quad (4.4.2)$$

$$\frac{\partial}{\partial\Gamma}b(0,x,\Gamma) = \frac{\partial}{\partial\Gamma}b_0(x) = 0, \quad (4.4.3)$$

where we define $\frac{d}{d\Gamma}f$ as the Gateaux derivative

$$\frac{d}{d\Gamma}f(\Gamma) = \lim_{\tau \to 0} \frac{f(\Gamma+\tau U) - f(\Gamma)}{\tau}$$

and U is an admissible probability density function. While the work below considers only two functions for the direction of the derivative, we note that a complete presentation would include a proof that $b(t,x,\Gamma)$ is in fact Gateaux differentiable at Γ. The calculations for this proof are straightforward, though somewhat tedious and left for future work.

If we denote $\frac{\partial}{\partial\Gamma}b(t,x,\Gamma)$ by $b_\Gamma(x,t,\Gamma)$, then we have

$$\dot{b}_\Gamma(x,t,\Gamma) = -\left(G(x)b_\Gamma(x,t,\Gamma)\right)_x + \frac{\partial}{\partial\Gamma}A(x,b(t,x,\Gamma)) + \frac{\partial}{\partial\Gamma}F(x,b(t,x,\Gamma),\Gamma). \tag{4.4.4}$$

Carrying out the derivatives of A and F yields

$$\begin{aligned}\frac{\partial}{\partial\Gamma}A(x,b(t,x,\Gamma)) &= \frac{1}{2}\int_{\underline{x}}^{x-\underline{x}} K_A(y,x-y)\left[b(t,y,\Gamma)b_\Gamma(t,x-y,\Gamma)+b_\Gamma(t,y,\Gamma)b(t,x-y,\Gamma)\right]dy\\ &\quad -\int_{\underline{x}}^{\overline{x}-x} K_A(x,y)\left[b(t,x,\Gamma)b_\Gamma(t,y,\Gamma)+b_\Gamma(t,x,\Gamma)b(t,y,\Gamma)\right]dy\end{aligned}$$

and

$$\begin{aligned}\frac{\partial}{\partial\Gamma}F(x,b(t,x,\Gamma),\Gamma) &= -\frac{1}{2}K_F(x)b_\Gamma(t,x,\Gamma)+\int_x^{\overline{x}} K_F(y)b_\Gamma(t,y,\Gamma)\Gamma(x,y)dy\\ &\quad +\int_x^{\overline{x}} K_F(y)b(t,y,\Gamma)\,U(x,y)\,dy\\ &= F(x,b_\Gamma(t,x,\Gamma),\Gamma)+\int_x^{\overline{x}} K_F(y)b(t,y,\Gamma)\,U(x,y)\,dy.\end{aligned}$$

Combining these results, the PDE for the function $b_\Gamma(t,x,\Gamma)$ is

$$\begin{aligned}\dot{b}_\Gamma(t,x,\Gamma) &= -\left(G(x)b_\Gamma(x,t,\Gamma)\right)_x \qquad (4.4.5)\\ &\quad +\frac{1}{2}\int_{\underline{x}}^{x-\underline{x}} K_A(y,x-y)\left[b(t,y,\Gamma)b_\Gamma(t,x-y,\Gamma)+b_\Gamma(t,y,\Gamma)b(t,x-y,\Gamma)\right]dy\\ &\quad -\int_{\underline{x}}^{\overline{x}-x} K_A(x,y)\left[b(t,x,\Gamma)b_\Gamma(t,y,\Gamma)+b_\Gamma(t,x,\Gamma)b(t,y,\Gamma)\right]dy\\ &\quad F(x,b_\Gamma(t,x,\Gamma),\Gamma)+\int_x^{\overline{x}} K_F(y)b(t,y,\Gamma)\,U(x,y)\,dy. \qquad (4.4.6)\end{aligned}$$

where $\Gamma(x, y)$ is the post-fragmentation density shown in Figure 4.3.1 (which we will call the **erosive** density), and $b(t, x, \Gamma)$ is the corresponding solution to Equations (3.2.1)-(3.2.3).

4.4.2 Sensitivity to uniform and binary fragmentation

We numerically solve Equation (4.4.5), and consider two specific post-fragmentation densities of interest for the function $U(x, y)$. First we examine the uniform density (denoted $\Gamma_U(x, y)$) which served as the seed for our optimization algorithm in the previous section. Our second density is the binary fragmentation commonly used in the literature to model the post-fragmentation density. This density (which we denote $\Gamma_B(x, y)$) assumes that fragmentation of a mother floc of size y results in two roughly equally-sized daughter flocs. This binary fragmentation is commonly thought of as a function "spike" at $x = y/2$ with a small distribution around it. To capture this behavior, it is typically implemented by either a uniform density on a small interval centered at $x = y/2$ or as a normal distribution with mean $\mu = y/2$ and small variance σ^2. We have chosen the latter implementation and approximate the binary fragmentation, conditioned on y, by a Gaussian density with mean $\mu = \frac{1}{2}(y - \underline{x})$ and variance $\sigma^2 = \frac{1}{20}(y - \underline{x})$. The variance was arbitrarily chosen to provide a small width to the density, illustrated in Figure 4.4.1. The uniform density is also illustrated in Figure 4.4.1 for comparison.

The numerical solutions to the sensitivity equations for each density are shown in Figures 4.4.2 and 4.4.3. Similar to the computations in the previous section, we used $Q = [0, 1]$ with $N = 30$ subintervals and the time interval $I = [t_0, t_f] = [0, 1]$ with $N_t = 50$ subintervals. All parameters were held fixed with the values listed in Table 4.1. The darker regions indicate the locations in t and x that are most sensitive to a change in Γ in the direction of the alternate density. When considering experimental design, these are the regions where it is most important to obtain accurate measurements because small changes in the measurements will yield the largest changes in the fitted post-fragmentation density.

For the uniform density (Figure 4.4.2), flocs near the minimum floc size are most

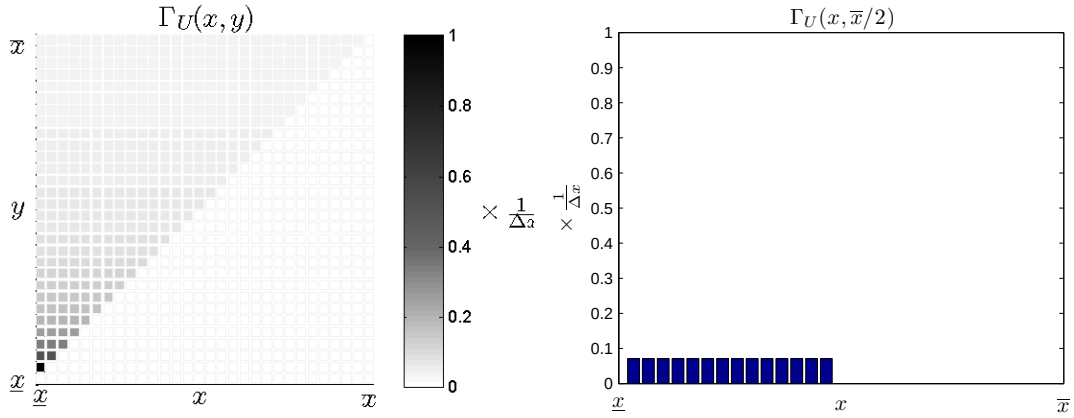

(a)

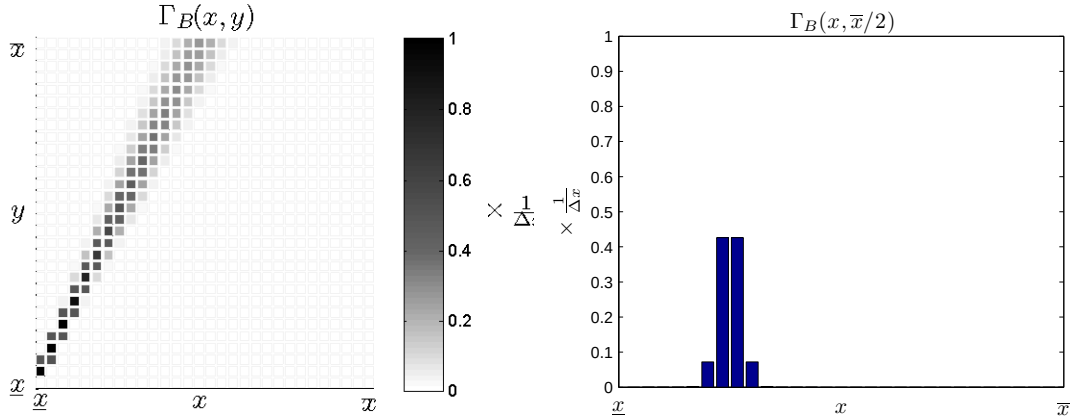

(b)

Figure 4.4.1: The two post-fragmentation densities of interest for the function $U(x, y)$ in the sensitivity equations (4.4.5): (a) uniform fragmentation, $\Gamma_U(x, y)$, and (b) binary fragmentation, $\Gamma_B(x, y)$. The height of the density is scaled by the step size, $\Delta x = (\overline{x} - \underline{x})/N$.

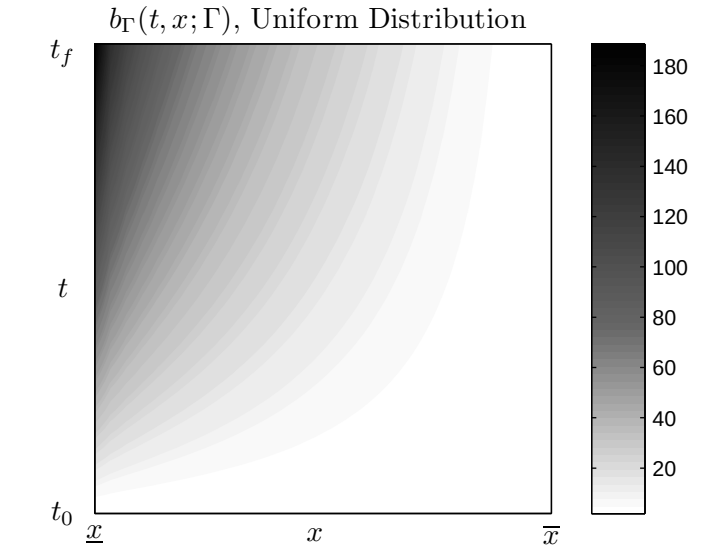

(a)

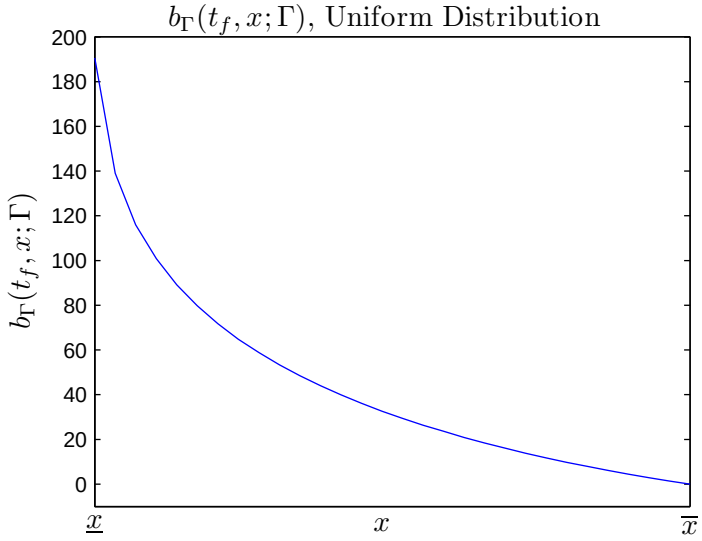

(b)

Figure 4.4.2: The solution $b_\Gamma(t, x, \Gamma)$ to the sensitivity equation (4.4.5) when considering changes in the post-fragmentation density Γ in the direction of the uniform density. (a) Contour plot of the values of $b_\Gamma(t, x, \Gamma)$ for $(t, x) \in [0, t_f] \times [\underline{x}, \overline{x}]$. Darker regions are more sensitive to the change in Γ in the direction of uniform fragmentation, suggesting population counts for small flocs at later times are most sensitive to Γ. (b) $b_\Gamma(t, x, \Gamma)$ evaluated at the final time t_f, where the highest sensitivities are found. The sensitivity decreases steadily with increasing floc size.

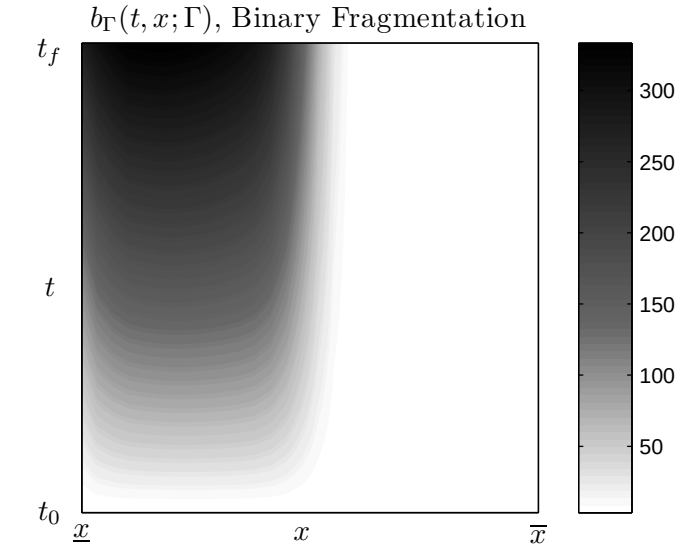

(a)

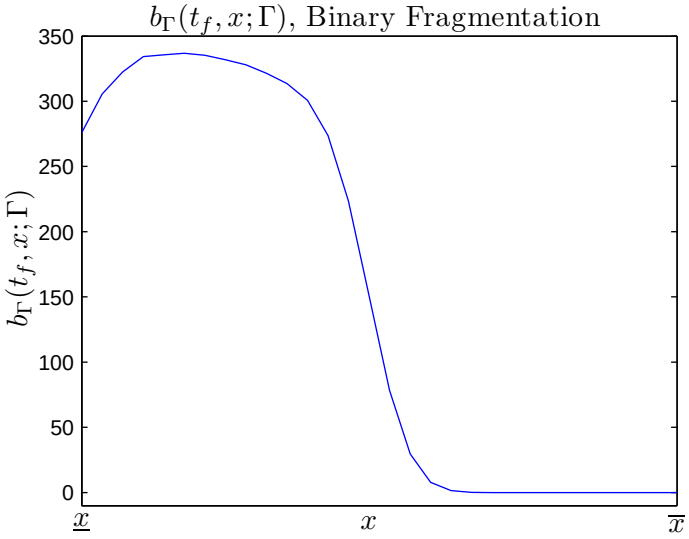

(b)

Figure 4.4.3: The solution $b_\Gamma(t, x, \Gamma)$ to the sensitivity equation (4.4.5) when considering changes in the post-fragmentation density Γ in the direction of the density representing binary fragmentation. (a) Contour plot of the values of $b_\Gamma(t, x, \Gamma)$ for $(t, x) \in [0, t_f] \times [\underline{x}, \overline{x}]$. Darker regions are more sensitive to the change in Γ in the direction binary fragmentation, suggesting population counts for flocs sized between $\underline{x}$ and $\overline{x}/2$ are most sensitive to Γ and this sensitivity increases with time. (b) $b_\Gamma(t, x, \Gamma)$ evaluated at the final time t_f, where the highest sensitivities are found. Sensitivity first increases, then decreases to zero by $x = \overline{x}/2$.

sensitive, and the sensitivity increases as time moves forward. We can justify this result by considering the differences in the two post-fragmentation densities. In the uniform density, a mother floc is equally probable to fragment into all possible daughter floc sizes. In contrast, the erosive density preferentially creates very small flocs in each fragmentation, regardless of mother floc size.

The results for the binary fragmentation density (Figure 4.4.3) show that flocs sized between $\underline{x}$ and $\overline{x}/2$ are most sensitive to Γ, and again the sensitivity increases with time. The restriction of any changes in the solution b to the left half of its domain is a direct result of the location of all of the mass in the binary fragmentation density. The binary fragmentation density is restricted to producing daughter flocs no bigger than roughly half the maximum floc size, and therefore all non-zero values of $\Gamma_B(x, y)$ are found only where $x < \overline{x}/2$.

4.5 Concluding Remarks

This chapter implemented the methodology presented in the the previous chapter for inferring the post-fragmentation density $\Gamma(x, y)$ from observed size-structured population data. Nonlinear constrained optimization was used to minimize the least squares cost functional between observed data and the fitted solution. We examined the optimization's robustness to both mesh size and noise in the data, yielding evidence that the best-fit Γ is sensitive to both. We also conducted a sensitivity analysis to better understand the sensitivity of the solution $b(t, x; \Gamma)$ to changes in Γ.

CHAPTER 5

CONCLUDING REMARKS & FUTURE DIRECTIONS

Flocculation is ubiquitous. Fragmentation, as one half of this general field of coalescent processes (encompassing both fragmentation and aggregation), is studied dramatically less than its partner despite exerting an equally important influence on a system's evolution. Communities of bacteria, metastatic cancers, social networks, voting blocs, and even the genetic history of species all fragment for different reasons. These phenomena are united by a common mathematical structure; a random process that separates one entity into many.

Pivotal to modeling the fragmentation of these aggregates is characterizing the floc sizes that result after a fragmentation event occurs. This post-fragmentation probability density of daughter flocs is one of the least well-understood aspects of flocculation. In this work, we have developed a mathematical methodology that uses high resolution structural data of **K. pneumoniae** bacterial flocs in suspension and knowledge of the hydrodynamic properties of fluids to construct a post-fragmentation probability density function of floc volumes [20]. An important contribution of this work is that the dominant fragmentation mechanism for medium to large flocs is erosion. It is **not** splitting of a floc into two similarly-sized daughter flocs, refuting the conventional assumption in the literature. As such, physicians can expect to see larger flocs circulate through the system longer than in the case of more symmetric fragmentation.

While this initial investigation is important, there are areas for improvement. For example, the bloodstream is a complex environment, and the numerical simulation of the

hydrodynamic forces on a floc is a challenging problem. Since the tumbling flocs in the flow experience highly variable forces over time, we can also rigorously test mechanistic hypotheses concerning viscoelasticity and mechanical hysteresis. Insights gained from these experiments can lead to model improvement,

As mentioned in Chapter 4, additional work can be conducted in the sensitivity analysis, especially when considering the sensitivity equations. Proof of the Gateaux differentiability will allow for a more general analysis of sensitivity, while examining solutions to the sensitivity equations around other common forms for the density (like the uniform and binary fragmentation models) with give greater insight into the influence the post-fragmentation density has on the population model. These investigations form a vital foundation for experimental design and comparison with laboratory data, facilitating a deeper understanding of floc fragmentation and its manifestation in populations of bacterial aggregates.

One intriguing aspect of this research is the novel use of the minimum spanning tree (MST) in Chapter 2 as a tool for inferring links between neighboring bacteria. Despite its connection to the underlying structure of the aggregate not being not well-understood, the approach proved quite fruitful. Deeper investigation into connections between the minimum spanning tree and the geometric and rheologic aspects of bacterial aggregates would put our approach on firmer ground. The MST has wide applicability and any insight gained would not only benefit the treatment of patients with disseminated bloodstream infections, but also a variety of other application areas, most notably those concerning geometry and structural environments such as polymers and proteins.

BIBLIOGRAPHY

[1] A. S. Ackleh. Estimation of parameters in a structured algal coagulation-fragmentation model. Nonlinear Analysis, Theory, Methods & Applications, 28(5):836–854, March 1997.

[2] A. S. Ackleh and B. G. Fitzpatrick. Modeling aggregation and growth processes in an algal population model: Analysis and computations. J. Math. Biology, 35:480–502, 1997.

[3] H.M. Adelman and R.T. Haftka. Sensitivity analysis of discrete structural systems. A.I.A.A. J., 24:823832, 1986.

[4] David J. Aldous. Deterministic and stochastic models for coalescence (aggregation and coagulation): a review of the mean-field theory for probabilists. Bernoulli, 5:1, 1999.

[5] Rick Aster, Brian Borchers, and Cliff Thurber. Parameter Estimation and Inverse Problems. Elsevier Academic Press, 2005.

[6] D. H. Bache. Floc rupture and turbulence: A framework for analysis. Chemical Eng. Science, 59:2521–2534, 2004.

[7] D. H. Bache. From rupture to structure: The physical character of flocs. Water Science & Technology, 12:55–62, 2004.

[8] Jacek Banasiak and Wilson Lamb. Coagulation, fragmentation and growth processes in a size structured population. Discrete and Continuous Dynamical Systems, 11:563, 2009.

[9] H. T. Banks and D. M. Bortz. A parameter sensitivity methodology in the context of hiv delay equation models. J. Math. Biol., 50:607, 2005.

[10] H. T. Banks and F. Kappel. Spline approximations for functional differential equations. Journal of Differential Equations, 34:496, 1979.

[11] H.T. Banks and K.L. Bihari. Modeling and estimating uncertainty in parameter estimation. Inverse Problems, 17:95–111, 2001.

[12] H.T. Banks and D.M. Bortz. Inverse problems for a class of measure dependent dynamical systems. Journal of Inverse & Ill-Posed Problems, 13:103–121, 2005.

[13] H.T. Banks and K. Kunisch. Estimation Techniques for Distributed Parameter Systems. Birkhauser, 1989.

[14] Patrick Billingsley. Convergence of Probability Measures. Wiley, 1968.

[15] Stefan Blaser. Break-up of flocs in contraction and swirling flows. Colloids & Surfaces A: Physicochemical & Engineering Aspects, 166:215–223, 2000.

[16] Stefan Blaser. Flocs in shear and strain flows. J. Colloid & Interface Science, 225:273–284, 2000.

[17] Stefan Blaser. Forces on the surface of small ellipsoidal particles immersed in a linear flow field. Chemical Engineering Science, 57:515–526, 2002.

[18] D. M. Bortz and Erin Byrne. Identification of the post-fragmentation probability measure in flocculation models. (In preparation), 2011.

[19] D. M. Bortz, T. L. Jackson, K. A. Taylor, A. P. Thompson, and J. G. Younger. Klebsiella pneumoniae flocculation dynamics. Bulletin of Mathematical Biology, 70:745–768, 2008.

[20] Erin Byrne, Steve Dzul, Michael Solomon, John Younger, and D.M. Bortz. The post-fragmentation density function for bacterial aggregates in laminar flow. Physical Review E, 83:04990, 2011.

[21] A.W. Cense, E.A.G. Peeters, B. Gottenbos, F.P.T. Baaijens, A.M. Nuijs, and M.E.H. van Dongen. Mechanical properties and failure of streptococcus mutans biofilms, studied using a microindentation device. Journal of Microbiological Methods, 67:463, 2006.

[22] Thomas H. Cormen, Charles E. Leiserson, Ronald L. Rivest, and Clifford Stein. Introduction to Algorithms. MIT Press and McGraw-Hill, 2nd edition edition, 2001.

[23] J.B. Cruz. System Sensitivity Analysis. Dowden Hutchinson & Ross, Inc., Stroudsburg, PA, 1973.

[24] Vincent T. DeVita, Theodore S. Lawrence, and Steven A. Rosenberg. Cancer: Principles and Practice of Oncology, volume 1. Lippincott Williams & Wilkins, 2008.

[25] Jay L. Devore. Probability and Statistics for Engineering and the Sciences. Thompson Brooks/Cole, 2004.

[26] Q. Du, C. Liu, and X. Wang. Retrieving topological information for phase field models. SIAM J. Applied Math., 65(6):1913–1932, 2005.

[27] S.P. Dzul, M.M. Thornton, D.N. Hohne, D.M. Bortz, M.J. Solomon, and J.G. Younger. Contribution of klebsiella pneumoniae capsule to bacterial community microstructure. Applied and Environmental Microbiology, submitted, 2010.

[28] M. L. Eggersdorfer, D. Kadau, H. J. Herrmann, and S. E. Pratsinis. Fragmentation and restructuring of soft-agglomerates under shear. J. Colloid & Interface Science, 342:261–268, 2010.

[29] Lyonel Ehrl, Miroslav Soos, and Marco Lattuada. Generation and geometrical analysis of dense clusters with variable fractal dimension. J. Phys. Chem. B, 113:1058710599, 2009.

[30] M. Eslami. Theory of Sensitivity in Dynamic Systems: An Introduction. Springer-Verlag, Berlin, 1994.

[31] Lawrence C. Evans. Partial Differential Equations. Graduate Studies in Mathematics. American Mathematical Society, 2000.

[32] Paul M. Frank. Introduction to Senstivity Theory. Academic Press, 1976.

[33] G. Frappier, B. S. Lartiges, and S. Skali-Lami. Floc cohesive force in reversible aggregation: A couette laminar flow investigation. Langmuir, 26(13):10475–10488, 2010.

[34] C.D. Gamma and C.L. Jimeno. Rock fragmentation control for blasting cost minimization and environmental impact abatement. In Rossmanith, editor, Rock Fragmentation by Blasting, page 273, 1993.

[35] R. Gateaux. Sur les fonctionnelles continues et les fonctionnelles analytiques. C.R. Acad. Sci. Paris Sr. I Math., 157:325–327, 1913.

[36] R. Gateaux. Fonctions d'une infinits des variables indpendante. Bull. Soc. Math. France, 47:70–96, 1919.

[37] Alison L. Gibbs and Francis Edward Su. On choosing and bounding probability metrics. International Statistical Review, 70:419, 2002.

[38] Gerhard Gottschalk. Bacterial Metabolism. Springer-Verlag, 2 edition, 1986.

[39] William W. Hager and Hongchao Zhang. A new active set algorithm for box constrained optimization. SIAM J. Optim., 17:526–557, 2006.

[40] Binbing Han, S. Akeprathumchai, S.R. Wickramasinghe, and X. Qian. Flocculation of biological cells: Experiment vs. theory. AIChE Journal, 49(7):1687–1701, July 2003.

[41] S. Havlin. Fractals in Physics. North-Holland, 1986.

[42] M. Hermawan, G. C. Bushell, V. S. J. Criag, W. Y. Teoh, and R. Amal. Floc strength characterization technique. an insight into silica aggregation. Langmuir, 20:6450–6457, 2004.

[43] Ko Higashitani and Kenji Iimura. Two-dimensional simulation of the breakup process of aggregates in shear and elongational flows. J. Colloid & Interface Science, 204:320–327, 1998.

[44] Ko Higashitani, Nobufumi Inada, and Toyohiko Ochi. Floe breakup along centerline of contractile flow to orifice. Colloids and Surfaces, 56:13–23, 1991.

[45] M. A. C. Huergo, M. A. Pasquale, A. E. Bolzn, , A. J. Arvia, and P. H. Gonzlez. Morphology and dynamic scaling analysis of cell colonies with linear growth fronts. Physical Review E, 82:031903, 2010.

[46] Neta Ilana, Michael Elkinb, and Israel Vlodavsky. Regulation, function and clinical significance of heparanase in cancer metastasis and angiogenesis. The International Journal of Biochemistry & Cell Biology, 38:2018, 2006.

[47] D. F. James, N. Yogachandran, M. R. Loewen, H. Liu, and A. M. J. Davis. Floc rupture in extensional flow. J. Pulp & Paper Science, 29(11):377–382, November 2003.

[48] P. Jarvis, B. Jefferson, J. Gregory, and S. A. Parsons. A review of floc strength and breakage. Water Research, 39(14):3121–3137, September 2005.

[49] P. Jarvis, B. Jefferson, and S. Parsons. The duplicity of floc strength. Water Science & Technology, 50(12):63–70, 2004.

[50] G.B. Jeffery. The motion of ellipsoidal particles immersed in a viscous fluid. Proceedings of the Royal Society A, 102:161–179, 1922.

[51] I.T. Jolliffe. Principal Component Analysis. Springer, New York, 2nd edition, 2002.

[52] J. L. Kelley. General Topology. Van Nostrand-Reinhold, Princeton, 1955.

[53] J. Kilander, S. Blomstrom, and A. Rasmuson. Spatial and temporal evolution of floc size distribution in a stirred square tank investigated using piv and image analysis. Chemical Eng. Science, 61:7651–7667, 2006.

[54] M. Kleiber, H. Antunez, T.D. Hien, and P. Kowalczyk. Parameter Sensitivity in Nonlinear Mechanics: Theory and Finite Element Computations. John Wiley & Sons, New York, NY, 1997.

[55] M. Kobayashi. Breakup and strength of polystyrene latex flocs subjected to a converging flow. Colloids & Surfaces A: Physicochemical & Engineering Aspects, 235(1-3):73–78, 2004.

[56] M. Kobayashi. Strength of natural soil flocs. Water Research, 39(14):3723–3278, September 2005.

[57] A. N. Kolmogoroff. On the log-normal distribution of particles sizes during break-up process. Dokl. Akad. Nauk SSSR, 31:99, 1941.

[58] V. Korstgens, H.C. Flemming, J. Wingender, and W. Borchard. Uniaxial compression measurement device for investigation of the mechanical stability of biofilms. Journal of Microbiological Methods, 46:9–17, 2001.

[59] Joseph Kruskal. On the shortest spanning subtree of a graph and the traveling salesman problem. Proceedings of the American Mathematical Society, 7(1):48–50, Feb 1956.

[60] H. Lamb. Hydrodynamics. Cambridge University Press, Cambridge, 1932.

[61] C. F. Lu and L. A. Spielman. Kinetics of floc breakage and aggregation in agitated liquid suspensions. J. Colloid & Interface Science, 103:95, 1985.

[62] J. M. Matsen, J. A. Spindler, and R. O. Blosser. Characterization of Klebsiella isolates from natural receiving waters and comparison with human isolates. Appl Microbiol, 28:672–678, 1974.

[63] I. N. McCave. Size-spectra and aggregation of suspended particles in the deep ocean. Deep-Sea Research, 31:329–352, 1984.

[64] Avrom I. Medalia. Dynamic shape factors of particles. Powder Technology, 4:117–138, 1970.

[65] A. Mohraz and M.J. Solomon. Direct visualization of colloidal rod assembly by confocal micrscopy. Langmuir, 21:5298, 2005.

[66] Katta G. Murty. Linear Complementarity, Linear and Nonlinear Programming. Heldermann Verlag, 1988.

[67] Jorge Nocedal and Stephen J. Wright. Nonlinear Optimization. Springer-Verlag, 2006.

[68] J. D. Pandya and L. A. Spielman. Floc breakage in agitated suspensions: Theory and data processing strategy. J. Colloid & Interface Science, 90:517, 1982.

[69] S. J. Peng and R. A. Williams. Direct measurement of floc breakge in flowing suspensions. J. Colloid & Interface Science, 166:321–332, 1994.

[70] Per-Anders Persson, Roger Holmberg, and Jaimin Lee. Rock blasting and Explosives engineering. CRC Press, 1994.

[71] R. Podschun and U. Ullman. Klebsiella spp. as nosocomial pathogens: epidemiology, taxonomy, typing methods, and pathogenicity factors. Clin Microbial Rev, 11(4):589–603, 1998.

[72] A. T. Potanin. On the model of colloid aggregates and aggregating colloids. J. Chem. Phys., 96:9191, 1992.

[73] A. T. Potanin. On the computer simulation of the deformation and breakup of colloidal aggregates in shear flow. J. Colloid & Interface Science, 157:399–410, 1993.

[74] D. Ramkrishna. Population Balances: Theory and Applications to Particulate Systems in Engineering. Academic Press, 2000.

[75] D. T. Ray and R. Hogg. Agglomerate breakage in polymer-flocculated suspensions. J. Colloid & Interface Science, 116:256–268, 1987.

[76] Ryszard Rudnicki and Radoslaw Wieczorek. Fragmentation-coagulation models of phytoplankton. Bull. Pol. Acad. Sci. Math., 54:175–191, 2006.

[77] A. Saltelli, M. Ratto, T. Andres, F. Campolongo, J. Cariboni, D. Gatelli, M. Saisana, and S. Tarantola. Global Sensitivity Analysis: The Primer. John Wiley & Sons, 2008.

[78] James W. Sinko and William Streifer. A new model for age-size structure of a population. Ecology, 48:910–918, 1967.

[79] D. J. Smit, M. J. Hounslow, and W. R. Paterson. Aggregation and gelation: I. analytical solutions for cst and batch operation. Chemical Engineerirq Saence, 49:1025–1039, 1994.

[80] D. J. Smit, M. J. Hounslow, and W. R. Paterson. Aggregation and gelation: Ii. mixing effects in continuous flow vessels. Chemical Eng. Science, 49:3147–3167, 1994.

[81] D. J. Smit, M. J. Hounslow, and W. R. Paterson. Aggregation and gelation: Ill. numerical classification of kernels and case studies of aggregation and growth. Chemical Eng. Science, 50:849–862, 1995.

[82] M. Smoluchowski. Drei vortrge ber diffusion, brownsche molekularbewegung und koagulation von kolloidteilchen. Phys Z, 17:557–571,585–599, 1916.

[83] P. Somasundaran, V. Runkanan, and P.C. Kapur. Flocculation and dispersion of colloidal suspensions by polymers and surfactants: experimental and modeling studies. In Stechemesser and Dobias, editors, Coagulation and Flocculation, pages 767–803. CRC Press, 2005.

[84] R. C. Sonntag and W. B. Russell. Structure and breakup of flocs subjected to fluid stresses i: Shear experiments. J. Colloid & Interface Science, 113:399, 1986.

[85] Richard C. Sonntag and William B. Russell. Structure and breakup of flocs subjected to fluid stresses ii: Theory. J. Colloid & Interface Science, 115:378–389, 1987.

[86] R. A. Speers, T. D. Durance, M. A. Tung, and J. Tou. Colloidal properties of flocculent and nonflocculent brewing years suspensions. Biotechnology Progress, 9(3):267–272, 1993.

[87] P. T. Spicer and S. E. Pratsinis. Coagulation and fragmentation: Universal steady-state particle-size distribution. AIChE J., 42(6):1612–1620, 1996.

[88] Lisa G. Stanley and Dawn L. Stewart. Design Sensitivity Analysis: Computational Issues of Senstivity Equation Methods. SIAM, 2002.

[89] P. Stoodley, A. Jacobsen, B.C. Dunsmore, B. Purevdorj, S. Wilson, H.M. Lappin-Scott, and J.W. Costerton. The influence of fluid shear and alcl3 on the material properties of pseudomonas aeruginosa pao1 and desulfovibrio sp. ex265 biofilms. Water Science and Technology, 43(6):113–120, 2001.

[90] Walter A. Strauss. Partial Differential Equations: An Introduction. Wiley, 1992.

[91] J.-C. Su, S. Y. Liang, W. L. Liu, and T. S. Jan. Ceramic micro/nanoparticle size evolution in wet grinding in stirred ball mill. J. Manufacturing Science & Engineering, 126:779–786, November 2004.

[92] R. Sudarsan, K. Milferstedt, E. Morgenroth, and H. J. Eberl. Quantification of detachment forces on rigid biofilm colonies in a roto-torque reactor using computational fluid dynamics tools. Water Science & Technology, 52(7):149–154, 2005.

[93] N. Tambo and H. Hozumi. Physical characteristics of flocs-II. Strength of floc. Water Research, 13(5):421–427, 1979.

[94] Albert Tarantola. Inverse problem theory and methods for model parameter estimation. SIAM, 2005.

[95] D. N. Thomas, S. J. Judd, and N. Fawcett. Flocculation modeling: A review. Water Research, 33(7):1579–1592, 1999.

[96] V. A. Tolpekin, M. H. G. Duits, D. van den Ende, and J. Mellema. Aggregation and breakup of colloidal particle aggregates in shear flow, studied with video microscopy. Langmuir, 20:2614–2627, 2004.

[97] R. Tomovic and M. Vukobratovic. General Sensitivity Theory. Elsevier Academic Press, New York, NY, 1972.

[98] A. W. van der Vaart. Asymptotic Statistics. Cambridge University Press, Cambridge, 1998.

[99] N. D. Vassileva, D. van den Ende, F. Mugele, and J. Mellema. Restructuring and break-up of two-dimensional aggregates in shear flow. Langmuir, 22:4959–4967, 2006.

[100] A Wierzbicki. Models and Sensitivity of Control Systems. Number 5 in Studies in Automation and Control. Elsevier Science Publishing Company, New York, NY, 1984.

[101] T. A. Witten and L. M. Sander. Diffusion-limited aggregation, a kinetic critical phenomenon. Physical Review Letters, 47:1400–1403, 1981.

[102] Jeffrey B. Wyckoff, Joan G. Jones, John S. Condeelis, and Jeffrey E. Segall. A critical step in metastasis: In vivo analysis of intravasation at the primary tumor. Cancer Research, 60:2504, May 2000.

[103] A. K. C. Yeung and R. Pelton. Micromechanics: A new approach to stuyding the stregth and breakup of flocs. J. Colloid & Interface Science, 184:579–585, 1996.

[104] Yuan Yuan and Ramin R. Farnood. Strength and breakage of activated sludge flocs. Powder Technology, 199(2):111 – 119, 2010.

APPENDIX A

FORMULATIONS OF χ_K AND A

The following formulations for χ_k and $\mathbf{A}$ were adapted from Blaser [17]. For the ellipsoid $D: \ \frac{x^2}{a_1^2}+\frac{y^2}{a_2^2}+\frac{z^2}{a_3^2}=1$ where $a_1 > a_2 > a_3$, let $r_1 = \frac{a_1}{a_3}$, $r_2 = \frac{a_2}{a_3}$, and $r_3 = 1$. Then the quantity χ_k is given by:

$$\chi_k = \int_0^\infty \frac{u\,du}{(r_k^2+u^2)\sqrt{(r_1^2+u^2)(r_2^2+u^2)(r_3^2+u^2)}}. \tag{A.0.1}$$

To define the matrix $\mathbf{A}$, let us first define the additional quantities $\chi_k\prime$ and $\chi_k\prime\prime$:

$$\chi_k\prime = \int_0^\infty \frac{u\,(r_k^2+u^2)\,du}{\left[(r_1^2+u^2)(r_2^2+u^2)(r_3^2+u^2)\right]^{3/2}} \tag{A.0.2}$$

$$\chi_k\prime\prime = \int_0^\infty \frac{u^3\,(r_k^2+u^2)\,du}{\left[(r_1^2+u^2)(r_2^2+u^2)(r_3^2+u^2)\right]^{3/2}}. \tag{A.0.3}$$

Using these definitions, the elements of $\mathbf{A}$ are given by:

$$\begin{aligned} A_{i,i} &= \frac{1}{d}\sum_{k=1}^{3}\alpha_k\,\chi_k\prime\prime\,E_{k,k} \\ A_{i,j} &= \frac{-\chi_j\,E_{i,j}+r_i^2\,\chi_k\prime\left(\Omega_{i,j}+\omega_p^k\right)}{2\chi_k\prime\left(r_i^2\chi_i+r_j^2\chi_j\right)}, \quad k\in\{1,2,3\},\ k\neq i,j \end{aligned} \tag{A.0.4}$$

where

$$\begin{aligned} \alpha_k &= \begin{cases} 2, & k = i \\ -1, & k \neq i \end{cases} \\ d &= 6\left(\chi_1'' \chi_2'' + \chi_2'' \chi_3'' + \chi_1'' \chi_3''\right). \end{aligned}$$

APPENDIX B

ALGORITHM PSEUDOCODE

The following pseudocode is a more detailed description of the algorithm from Chapter 1, Section 2.2.5 used to construct the post-fragmentation density functions from the 3D positional data for the flocs.

INPUT $Flocs$ = list of flocs
        γ = fluid shear rate
        σ_r = biofilm rupture stress

i = 0
WHILE i $\leq$ (No. of flocs in $Flocs$)
        $\mathbf{X}$ = centers of mass for bacteria in $Flocs(i)$
        $dist = \sqrt{\mathbf{X} * \mathbf{X}^{\mathrm{T}}}$
        $Edges$ = MST($\mathbf{X}$,**dist**)

        [$\mathbf{A}$, var] = PCA($\mathbf{X}$)
        $semiaxes = \sqrt{var}$;
        D = ellipsoid($semiaxes$)
        $\mathbf{f_R}$ = forces(D, γ)

        FOR $k = 1 :$ (No. of edges in $Edges$)

14 $Edge_k$ = kth longest edge

15 $P_\perp$ = $\perp$ bisector of $Edge_k$

16 $\mathbf{n}_\perp$ = normal to P$_\perp$

17 $$\mathbf{F}_\perp = \left| \iint_{D>P_\perp} \mathbf{f}_\mathrm{R} \cdot \mathbf{n}_\perp \, d\sigma \right| + \left| \iint_{D<P_\perp} \mathbf{f}_\mathbf{R} \cdot \mathbf{n}_\perp \, d\sigma \right|$$

18 $$\sigma_{\max} = \frac{\mathbf{F}_\perp}{\mathrm{area}(D \bigcap P_\perp)}$$

19 IF $\sigma \geq \sigma_r$

20 REMOVE $Edge_k$ from $Edges$

21 ADD daughter flocs TO $Flocs$

22 BREAK

23 END IF

24 IF k = (No. of edges in $Edges$)

25 ADD $Flocs(i)$ TO Unfragmented Flocs

26 END IF

27 END FOR

28 i = i + 1

29 END WHILE